SLAC–PUB–4656
June 1988
E/T

Physics With Polarized Electron Beams*

MORRIS L. SWARTZ

Stanford Linear Accelerator Center
Stanford University, Stanford, California, 94309

Presented at the SLAC Summer Institute
on Particle Physics, Stanford, Ca.,
Aug. 10-21, 1987

* Work supported by the Department of Energy, contract DE–AC03–76SF00515.

Introduction

As a distinct field, elementary particle physics is now approximately forty years old. In all that time, only a few of the thousands of experiments that have been performed have made use of spin polarized particle beams (with apologies to those who have studied neutrino interactions, we choose to define the term *polarized beam* to refer to the case in which the experimenter has control over the polarization direction). If we restrict the discussion to spin polarized electron beams, the number of experiments becomes countable with the fingers of one hand (with several to spare)! There are two reasons for this lack of interest. The first is that spin polarized beams are difficult to produce, accelerate, and transport. The second reason is that any physical process that can occur during the collision of a polarized particle with another (polarized or not) can also occur during the collision of unpolarized particles. One might ask then, why has any effort been expended on the subject? The answer, at least in the case of polarized electron beams, is that electron accelerators and storage rings have in recent years achieved sufficient energy to begin to probe the weak interaction directly. The weak interaction distinguishes between left- and right-handed fermionic currents. Left-handed particles interact in a fundamentally different way than their right-handed counterparts. If the experimenter wishes to explore or exploit this difference, he (or she) must either prepare the spin state of the incident particles or analyze the spin state of outgoing particles. For reasons of generality and improved statistical precision, the former is usually preferable to the latter.

The first of these lectures will review some of the techniques necessary for the production, transport, and monitoring of polarized electron (or positron) beams. The second lecture will survey some of the physics possibilities of polarized electron-positron collisions.

LECTURE I: EXPERIMENTAL TECHNIQUES

1. Definitions

Before discussing the gory experimental details of polarized electron physics it is worthwhile to review a few simple definitions. Let's consider an ensemble of electrons at rest. We can define a function f of some arbitrary direction (given by the unit vector $\hat{n}$) as the difference between the number of electrons that have spin parallel to $\hat{n}$ and the number of those that have spin anti-parallel to $\hat{n}$, normalized to the total number of electrons,

$$f(\hat{n}) = \frac{N_e(spins\ parallel\ \hat{n}) - N_e(spins\ anti-parallel\ \hat{n})}{N_e(spins\ parallel\ \hat{n}) + N_e(spins\ anti-parallel\ \hat{n})}. \tag{1.1}$$

Let $\hat{s}$ be the direction for which f is maximum, then the polarization of the ensemble is defined as

$$\vec{P} = f(\hat{s})\hat{s}. \tag{1.2}$$

Note that the magnitude of $\vec{P}$ represents the fraction of the ensemble that is polarized.

Under Lorentz transformations, $\hat{s}$ (and $\vec{P}$) transforms like the space component of a contravariant 4-vector. In the rest frame of the ensemble, we can write the spin 4-vector s^μ_{cm} as

$$s^\mu_{cm} = \begin{pmatrix} 0 \\ \hat{s} \end{pmatrix}. \tag{1.3}$$

The spin 4-vector is therefore orthogonal to the momentum 4-vector. We can use this fact to write s^μ in an arbitrary frame as

$$s^\mu = \begin{pmatrix} \gamma\vec{\beta}\cdot\hat{s} \\ \hat{s} + \frac{\gamma^2}{\gamma+1}\vec{\beta}\cdot\hat{s}\vec{\beta} \end{pmatrix} \tag{1.4}$$

where γ and $\vec{\beta}$ are the familiar Lorentz parameters describing ensemble boost and velocity, and $\hat{s}$ is the rest frame spin vector. Note that since $\hat{s}$ defines an

intrinsic property of each particle, s^μ has physical meaning only in the rest frame and is used only for constructing Lorentz invariant quantities.

The spin direction of a particle or ensemble is the subject of considerable terminology and sometimes, much confusion. A distinction must be made between the term polarization as applied to fermions and the term as applied to photons and other gauge bosons. *Longitudinally* polarized fermions have their spin vectors $\hat{s}$ colinear to their direction of travel. The spin direction may be parallel to the momentum direction (in which case the particle is *right-handed*) or antiparallel to the momentum direction (the particle is *left-handed*). These states are also called *helicity* states. If the spin vector is orthogonal to the direction of motion, the polarization is called *transverse.*

For photons and gauge bosons, the term polarization refers to a vector field which is related to the particle spin in a more complex manner. In this document, we shall only consider definite spin states. The state with photon spin along the particle direction will be called the *right-circularly polarized* state. The state with the photon spin antiparallel to the direction of motion will be called the *left-circularly polarized* state.* These states are also called *helicity* states. The reader who is easily confused can skip to the next section now. Otherwise, we note that the helicity states are special cases of transversely polarized photons. Not all transversely polarized photons are helicity states, of course. Longitudinally polarized photons are, naturally, spin 0 states.

Units

The units used in these lectures are Gaussian CGS. Usually, but not always, we will use the convention $\hbar = c = 1$. Occasionally, other units and conventions may slip in. Please accept my apologies in advance.

⋆ Note that particle physicists use a convention that is the opposite of that used by spectroscopists who (understandably) view the world as coming toward themselves.

2. Motion in Electromagnetic Fields

The acceleration and transport of our ensemble of electrons inevitably requires that we subject it to various electromagnetic fields. In general, the evolution of the polarization state in the presence of such fields is a quantum mechanical problem. However, if the frequencies of all fields are small as compared with the quantum precession frequency of the spin vector, we can treat the problem classically. The precession frequency ν_p (also called the Larmor frequency) is given by the following expression

$$\nu_p = \frac{geB_a}{4\pi m} \approx 2.8 \text{ MHz/gauss} \cdot B_a \tag{2.1}$$

where: g is the gyromagnetic ratio of the electron; e is the charge of the electron; m is the mass of the electron; and B_a is the applied magnetic field. Therefore, if the frequencies are less than RF or microwave frequencies, we can use a classical analysis. The classical evolution of a spin vector in the presence of an electromagnetic field is given by the BMT equation,[1]

$$\frac{ds^\mu}{d\tau} = \frac{e}{m}\left[\frac{g}{2}F^{\mu\nu}s_\nu + \left(\frac{g-2}{2}\right)V^\mu(s_\alpha F^{\alpha\beta}V_\beta)\right] \tag{2.2}$$

where: τ is the proper time, $F^{\mu\nu}$ is the electromagnetic field tensor, and V^μ is the velocity four-vector. While it is encouraging that the time evolution of the spin vector is described by a covariant equation, the BMT equation is inconvenient for practical calculations. Normally, we desire to calculate the rest frame spin orientation as a function of laboratory variables. This can be done by substituting Equation (1.4) into Equation (2.2) and grinding through a bit of algebra.† The result, originally derived by Thomas in 1927,[3] is

$$\frac{d\hat{s}}{dt} = \hat{s} \times \frac{e}{m}\left[\left(\frac{g-2}{2}+\frac{1}{\gamma}\right)\vec{B} - \left(\frac{g-2}{2}\right)\frac{\gamma}{\gamma+1}(\vec{\beta}\cdot\vec{B})\vec{\beta} - \left(\frac{g}{2}-\frac{\gamma}{\gamma+1}\right)\vec{\beta}\times\vec{E}\right] \tag{2.3}$$

where t is the laboratory time variable and $\vec{B}$, $\vec{E}$ are the laboratory magnetic

† The interested reader is invited to follow the details of the calculation in Jackson,[2] pp 558-559.

and electric fields. Since the fields experienced by a particle depend upon its trajectory and since we often desire to know the spin direction relative to the direction of motion of the particle, it is essential that we also solve the equations of motion for the particle momentum $\vec{p}$ and energy $\mathcal{E}$,

$$\begin{aligned} \frac{d\vec{p}}{dt} &= e\left[\vec{E} + \vec{\beta} \times \vec{B}\right] \\ \frac{d\mathcal{E}}{dt} &= e\vec{\beta} \cdot \vec{E}. \end{aligned} \tag{2.4}$$

The solutions of Equations (2.3) and (2.4) can, in general, be quite complex. While numerical solutions are usually required for practical problems, we can gain much intuitive understanding by considering three special cases:

1. $\vec{\beta}$ along $\vec{B}$, $\vec{E}$

If we assume that the particle motion is parallel to the direction of an electric and/or magnetic field, Equations (2.3) and (2.4) become

$$\begin{aligned} \frac{d\hat{s}}{dt} &= \hat{s} \times \left[\frac{e\vec{B}}{m\gamma}\right] \\ \frac{d\vec{p}}{dt} &= e\vec{E} \\ \frac{d\mathcal{E}}{dt} &= e\beta E. \end{aligned} \tag{2.5}$$

Equations (2.5) imply that the particle is accelerated along the electric field and that the spin vector precesses about the magnetic field direction at a rate given by the Lorentz-dilated rest frame rate.

2. $\vec{\beta}$ transverse to a $\vec{B}$ field

Since nearly all beam transport systems utilize magnetic dipole fields, this case is very important. The equations of motion for a transverse magnetic field

are

$$\begin{aligned}
&\frac{d\mathcal{E}}{dt} = 0 \\
&\frac{d\vec{p}}{dt} = \vec{p} \times \vec{\omega}_p, \quad \vec{\omega}_p = \frac{e}{\gamma m}\vec{B} \\
&\frac{d\hat{s}}{dt} = \hat{s} \times \vec{\omega}_s, \quad \vec{\omega}_s = \frac{e}{m}\Big(\frac{g-2}{2} + \frac{1}{\gamma}\Big)\vec{B}.
\end{aligned} \tag{2.6}$$

We observe that both the momentum vector and perpendicular component of the spin vector (to the magnetic field) rotate about an axis defined by the magnetic field direction. Note, however, that the rotation frequencies are different. If we assume that the spin vector lies in the same plane as the momentum vector, then we can write that the angular difference occurring after a time T is

$$\Delta\theta = \int_0^T (\omega_s - \omega_p)dt = \frac{e}{m}\Big(\frac{g-2}{2}\Big)\int_0^T Bdt. \tag{2.7}$$

The integral of the magnetic field over the path of the particle is related to the bend angle of the particle trajectory θ_b by the expression,

$$\theta_b = \frac{e}{\gamma m}\int_0^T Bdt. \tag{2.8}$$

We can therefore rewrite Equation (2.7) as

$$\Delta\theta = \Big(\frac{g-2}{2}\Big)\gamma\theta_b. \tag{2.9}$$

Don't be mislead by the simple appearance of Equation (2.9). It has enormous physical content. Note that if the gyromagnetic ratio of the electron were exactly two, the spin vector would exactly follow the momentum vector as the particle passed through the transverse, but not necessarily uniform, magnetic field. As we know, the electron g-factor deviates from two due to virtual quantum corrections.

This causes the spin vector to precess as the electron passes through the field. The factor a,

$$a \equiv \frac{g-2}{2} = (1.159652209 \pm 0.000000031) \times 10^{-3}$$

is called the *anomalous magnetic moment* of the electron and is one of the most precisely measured physical constants of nature. Although a is quite small, the γ factor of a high energy electron beam can be quite large ($\gamma \approx 10^5$ at 50 GeV) and the precession of the spin vector can be considerable. This phenomenon is a substantial nuisance to anyone attempting to transport a spin polarized electron beam.

Equation (2.9) has enabled very precise measurements of the muon magnetic moment. These experiments work by trapping polarized muons in a storage ring and detecting the decay electrons. The spin precession causes a modulation of the electron momentum spectrum. By measuring the modulation rate, it is possible to infer the precession rate and therefore the anomalous magnetic moment.

We shall see in the next chapter that Equation (2.9) is responsible for the presence of depolarizing spin resonances in electron-positron storage rings. These resonances have been used to calibrate the energy scale of most operational machines. Indeed, the masses of many heavy vector mesons have been measured to within few parts in 10^5 with this technique.

3. $\vec{\beta}$ transverse to an $\vec{E}$ field

Let's assume that our electron traverses a transverse electric field for a sufficiently short time, that it is deflected but not accelerated. The equations of motion for this case are

$$\begin{aligned} \frac{d\mathcal{E}}{dt} &= 0 \\ \frac{d\vec{p}}{dt} &= e\vec{E} \\ \frac{d\hat{s}}{dt} &= \hat{s} \times \vec{\omega}_s, \quad \vec{\omega}_s = \frac{e}{m}\left(\frac{g}{2} - \frac{\gamma}{\gamma+1}\right)\vec{\beta} \times \vec{E}. \end{aligned} \tag{2.10}$$

After traversing the field for a time T, the particle is deflected by an angle θ_b where

$$\theta_b = \frac{eET}{p} = \frac{eET}{\gamma m \beta}. \tag{2.11}$$

Assuming that the spin vector lies in the plane defined by the electric field and the velocity vector, it is rotated in the same direction as $\vec{\beta}$ by an angle θ_s where

$$\theta_s = \omega_s T = \frac{e\beta ET}{m}\left(\frac{g}{2} - \frac{\gamma}{\gamma+1}\right). \tag{2.12}$$

Subtracting the above two equations, we can then write that the angular precession $\Delta\theta$ is

$$\Delta\theta = \theta_s - \theta_b = \left[\left(\frac{g-2}{2}\right)\gamma - \frac{1}{\gamma}\frac{g}{2}\right]\theta_b. \tag{2.13}$$

We note that as $\gamma \rightarrow 1$, the precession angle becomes $\Delta\theta = -\theta_b$. The spin vector remains undeflected. Low energy electrons become depolarized as they pass through matter because multiple scattering randomizes their directions but not their spins. For $\gamma \gg 1$, Equation (2.13) becomes identical to Equation (2.9) and the precession is the same as for a transverse magnetic field.

3. Polarized Electron Sources

Polarized electron sources have been under development for quite some time. Since a proper survey of all known techniques could easily fill the entire content of these two lectures, we shall discuss only the two techniques currently being used at electron accelerators. The reader who is interested in a more complete description of the field is referred to the extensive literature that is available.

It is worth mentioning at this point, that the traditional Stern-Gerlach filter does not work for charged beams. The reader will recall that Stern and Gerlach performed their classic experiment by passing a beam of neutral silver atoms through an inhomogenous magnetic field. The only force acting upon the atoms

was that due to the coupling of the atomic magnetic moment with the gradient of the field. Since the two spin states of the $J = 1/2$ ground state have opposite magnetic moments, the beam was split into two transversely polarized beams. Unfortunately, the Lorentz force and the uncertainty principle conspire to destroy the effect for charged particles.*†

In 1976, Pierce and Meier[9] observed the photoemission of polarized electrons from negative electron affinity gallium arsenide (NEA GaAs). Since then, nearly all polarized electron sources that have been used with accelerators have been based on this technique. These sources have the advantages of relative simplicity, easy reversibility, and good beam characteristics, but are limited to a maximum polarization of fifty percent. They will be described in the first section of this chapter.

The other source of polarized electrons that figures prominently in current planning is the storage ring. The emission of synchrotron radiation causes the slow buildup of transverse polarization in nearly all suitably tuned machines. As was mentioned in the last chapter, this phenomenon has enabled the precise calibration of all of the electron-positron storage rings that are now in operation. It is currently planned to use this technique to produce longitudinally polarized beams at the HERA electron-proton collider. Much study has been devoted to the possible polarization of the LEP electron-positron storage ring. It is sufficient to say that the feasibility of polarization at LEP is unclear. The second section of this chapter will discuss the theory of storage ring polarization in its simplest (and most naive) form.

⋆ The interested reader can find this discussed in Baym,[7] pp 324-330, and in Kessler,[8] pp 2-6.

† Many sources of polarized electron beams have made use of Stern-Gerlach filters to state select beams of neutral atoms. The atoms are then ionized to produce polarized electrons. While such sources have achieved high beam polarization, they usually employ magnetic and/or electric fields in a region traversed by low energy electrons. The effect is to increase the emittance and/or energy spread of these sources which tends to make them unsuitable for use with accelerators.

3.1. GALLIUM ARSENIDE SOURCES

Gallium arsenide is a well-known semiconductor with two very important properties that make it useful as a polarized electron source:

1. Its band structure permits a given spin state to be preferentially pumped into the conduction band.

2. Its surface can be treated to develop a negative work function (hence the term, *negative electron affinity*).

The band structure of GaAs at the energy maximum of the valence band and energy minimum of the conduction band is shown in Figure 1. The band energy versus momentum is shown on the left-hand side and the energy level structure is shown on the right-hand side of the figure. We note that the band gap of the material is $E_g = 1.52\ eV$. At the minimum of the conduction band and the maximum of the valence band, the electron wavefunctions have S and P symmetry, respectively. Spin-orbit splitting causes the $P_{3/2}$ states to reside in energy above the $P_{1/2}$ states by an amount $\Delta = 0.34\ eV$. The selection rules for the absorption of right- and left-handed circularly polarized photons are $\Delta m_j = +1$ and $\Delta m_j = -1$, respectively. The selection rules are indicated by the solid and dashed arrows in Figure 1. The reader will recall from undergraduate quantum mechanics that these electric dipole transitions proceed via an operator that changes the orbital angular momentum of the inital state by one unit. The spin of the electron remains unchanged in the process.

Let's consider what happens when a right-circularly polarized photon is incident upon a GaAs crystal. The photon direction is the only vector in the system. All angular momentum projections refer to the incident photon direction. If the photon energy E_γ is in the range $E_g \leq E_\gamma \leq E_g + \Delta$, then transitions can only occur from the $P_{3/2}$ states to the $S_{1/2}$ states. Specifically, the P state with $m_j = -3/2$ can make a transition to the S state with $m_j = -1/2$ and the P state with $m_j = -1/2$ can make a transition to the S state with $m_j = +1/2$. In

the former case, the emitted electron has spin antiparallel to the incident photon direction (or parallel to its ejected direction). In the latter case, the spin of the emitted electron is parallel to the incident photon direction (antiparallel to its ejected direction). Due to Clebsch-Gordon coefficients (the P state with $m_j = -3/2$ is a pure spin state whereas state with $m_j = -1/2$ is not), the former transition is three times more likely than the latter. The relative transition rates are indicated by circled numbers in Figure 1. This implies that the absorption of a right circularly polarized photon produces a right-handed electron with a polarization

$$P = \frac{3-1}{3+1} = 50\%. \tag{3.1}$$

Actually, all we've shown so far is that we can create polarized electrons in the conduction band with a beam of circularly polarized photons. In order to make a polarized source, the electrons must leave the material. In normal GaAs, the energy gap from the bottom of the conduction band to the free electron state is approximately 2.5 electron volts. Even with a large applied electric field, pure GaAs is a poor photoemitter. The magic that is necessary to make it an efficient photoemitter is shown in Figure 2. The energy of the various bands is shown as a function of depth near the surface for several materials: pure GaAs, GaAs with a cesiated surface, and GaAs with a surface layer of Cs_2O . The energy of the free electron state is shown as E_∞. The addition of cesium to the surface causes the energy gap between the conduction band and the free electron state to decrease to zero. The addition of Cs_2O to the surface causes the gap to become negative! Quantum efficiencies* as large as 5% have been been observed for GaAs photocathodes that have been treated with Cs_2O (actually CsF is currently used instead). At photon energies that are appropriate for polarized electron production, quantum efficiencies in the range $0.1\% \rightarrow 0.5\%$ are typical.

---

* The definition of quantum efficiency is the probability that an electron is emitted when a photon is incident upon the photocathode surface.

In practice, the photoexcited electrons can become depolarized from spin flip scattering processes that occur before emission from the photocathode. The result of an actual measurement of P as a function of photon energy is shown in Figure 3. We note that the polarization increases to a value in the range $40\% \rightarrow 45\%$ as the photon energy is decreased. Although the systematic error in such measurements is typically 10%, the degradation of the polarization from the theoretical 50% is well established.

The Future

The development of the polarized photoemission source is still continuing.[4] Much work has gone into improving the polarization, efficiency, and lifetime of GaAs sources. Another very interesting direction involves the development of semiconductor materials with band structures that are capable of providing completely polarized beams. Much work has already gone into the investigation of the $II-IV-V_2$ family of chalcopyrite semiconductors. Members of this family have a band structure that does not have a polarization defeating degeneracy. The band structure of one such semiconductor is shown in Figure 4. In principle, such materials can provide electrons of 100% polarization. However, to be useful as a high current source of electrons, a material must possess several other properties. A relatively large bandgap is important both for optical pumping reasons and because it is necessary to make NEA surfaces. Good physical and chemical properties are also required. To date, no good rival for GaAs has been developed.

3.2. Storage Rings

It has been known since the early 1960's that the emission of synchrotron radiation could lead to the gradual *transverse* polarization of the beams in electron-positron storage rings.[10] A small fraction of the synchrotron radiation emitted by the circulating electrons and positrons causes them to change their spin states. Effectively, the particles make magnetic dipole transitions to the lower energy state (all magnetic moments aligned with the guide field). The electron spins

preferentially become antiparallel to the magnetic field and the positron spins become parallel to the field. This physical picture is somewhat too naive.† The interested reader is referred to an excellent review article by Jackson[11] for more details.

The correct and general result for the spin flip probability per unit time was first derived by Baier and Katkov,[12]

$$\Gamma^{\uparrow\downarrow} = \frac{5\sqrt{3}}{16}\frac{e^2\hbar}{m^2c^5}\gamma^5|\dot{\vec{\beta}}|^3\left[1 - \frac{2}{9}\left(\hat{s}\cdot\hat{\beta}\right)^2 + \frac{8\sqrt{3}}{15}\hat{s}\cdot\left(\hat{\beta}\times\dot{\hat{\beta}}\right)\right] \tag{3.2}$$

where $\hat{s}$ refers to the spin of the particle before the transition and the $\uparrow\downarrow$ superscripts refer to the spin direction after the transition. We can substitute this expression into the time evolution equation for the number of electrons with spin antiparallel to the guide field,

$$\frac{dN_\downarrow}{dt} = \Gamma^\downarrow N_\uparrow - \Gamma^\uparrow N_\downarrow \tag{3.3}$$

where $N_\downarrow$ ($N_\uparrow$) is the number of electrons with spin antiparallel (parallel) to the guide field. For simplicity, let's assume that the ring is circular and that $\dot{\vec{\beta}} = -c\hat{\rho}/\rho$ where ρ ($\hat{\rho}$) is the radius (radius unit vector) of the ring. Solving Equation (3.3), we can write that the polarization of the storage ring as a function of time is

$$P(t) = \frac{N_\downarrow - N_\uparrow}{N_\downarrow + N_\uparrow} = P_\circ\left(1 - e^{-t/t_\circ}\right). \tag{3.4}$$

The polarization approaches an asymptotic value $P_\circ$ with a characteristic time $t_\circ$. These parameters are

$$\begin{aligned} P_\circ &= \frac{8}{5\sqrt{3}} = 0.9238 \\ t_\circ &= \left[\frac{5\sqrt{3}}{8}\frac{e^2\hbar\gamma^5}{m^2c^2\rho^3}\right]^{-1}. \end{aligned} \tag{3.5}$$

Note that the maximum polarization obtainable in a storage ring is 92%.

† Note that if the electron gyromagnetic ratio were less than 1.2, the opposite spin orientations would result... so much for simple pictures.

This is very much an idealized number since it assumes that the only depolarizing process is reverse spin flip synchrotron emission. The expression for $t_\circ$ has been written to simplify its generalization to a real storage ring. In a real machine, the bending radius of the the dipole magnets differs from the average radius of the particle orbits. In a correct treatment, one must replace ρ^{-3} with its average, taken over a closed orbit. For a storage ring consisting only of identical bending magnets of bending radius ρ and straight sections, we can write that

$$\rho^{-3} \rightarrow \langle \rho^{-3} \rangle_{avg} = (\frac{\rho}{R})\rho^{-3} \tag{3.6}$$

where R is the average orbit radius. Substituting Equation (3.6) into the expression for $t_\circ$, we can write that the polarizing time is

$$t_\circ(sec) = 98.66 \frac{[\rho(m)]^3}{[\mathcal{E}(GeV)]^5} \frac{R}{\rho}. \tag{3.7}$$

To get a feeling for the magnitude of $t_\circ$, let's consider several machines:*

Table I

Machine	Beam Energy	Polarizing Time
SPEAR	4 GeV	10 min.
HERA	30 GeV	20 min.
LEP	46.5 GeV	300 min.
SLC Damping Ring	1.21 GeV	15 min.

We note that these times are enormous as compared with most of the time scales that govern storage ring operation. The reason is that the spin flip photon emissions are a tiny fraction of the total synchrotron radiation emission. The

* The proposed installation of wiggler magnets into LEP would reduce the average bend radius and therefore, the polarizing time to 90 minutes.

ratio of the power radiated in spin flip transitions to the power radiated in spin conserving emissions, $\mathcal{R}$, is given by the expression

$$\mathcal{R} = 3\left(\frac{\hbar\gamma^2}{mc\rho}\right)^2\left(1 \pm \frac{35\sqrt{3}}{64}\right) \tag{3.8}$$

where the two signs refer to the two spin flip directions. This number is normally quite small. For example, the value of the ratio for the SPEAR storage ring is $\mathcal{R} \simeq 10^{-11}$.

Depolarizing Effects

Thus far, we have discussed only the relatively simple physics that drives the polarizing process. We have remarked how subtle the process is and how slowly it proceeds. We must be concerned, therefore, that the system is quite sensitive to any depolarizing processes. If these proceed with a characteristic rate $1/t_d$, the asymptotic polarization P_∞ is reduced to

$$P_\infty = P_\circ \frac{1}{1 + t_\circ/t_d}. \tag{3.9}$$

The theory of depolarization in storage rings has advanced substantially in recent years.[6,13] Unfortunately, a complete description of it is beyond the scope of these lectures. What follows is a rather heurisitic description of the underlying physical processes.

The most dramatic depolarizing effects that occur in storage rings are spin resonances. Whenever the circulating electrons see any electromagnetic disturbance that has a substantial Fourier component at the spin precession frequency or at an integral multiple of it, resonant spin flipping can occur. Using Equation (2.9), we can write that the number of spin precessions per orbit of each particle, ν (called the spin tune of the machine), is given by the expression

$$\nu = \left(\frac{g-2}{2}\right)\frac{\mathcal{E}}{m} = \frac{\mathcal{E}(MeV)}{440.65}. \tag{3.10}$$

It is clear that whenever ν is an integer, all of the machine imperfections will conspire to produce a strong depolarizing resonance. The spacing between the

primary resonances is fixed at 440 MeV. This fact causes major problems for very high energy storage rings like LEP. The energy spread of the stored beams is normally a fixed fraction of the beam energy. As a machine becomes more energetic, the energy spread becomes a larger fraction of 440 MeV and it becomes progressively more difficult to avoid resonances.

Unfortunately, the beam orbit is not the only periodic phenonemon in the storage ring. The beams make betatron oscillations and experience energy oscillations. The horizontal (vertical) betatron tune ν_x (ν_y) is the number of such oscillations per orbit. The synchrotron tune ν_s refers to the number of energy oscillations per orbit. The condition for these effects to produce disturbances that are phased with the Larmor precession is

$$\nu = n \pm i\nu_x \pm j\nu_y \pm k\nu_s$$

where n, i, j, k are integers. The resonances for which $i, j, k = 0$ are called primary resonances and those for which they are nonzero are called sideband resonances. Since ν_x and ν_y are normally greater than one, there are several sideband resonances between the primary resonances. The sideband resonances are normally much weaker than the primaries. This fact makes them useful for calibration purposes (the primary resonances are very broad).

Even if our storage ring is carefully tuned to avoid resonances, other processes can cause depolarization. Since the beam has a transverse emittance, the particles are subject to random transverse fields. These can cause depolarization. Similarly, the passage of one beam through the other produces magnetic fields which can cause mutual depolarization. In practice, the measured polarization of a storage ring never exceeds $\sim 70\%$. Even then, some witchcraft in the tuning of the machine is often required.

Longitudinal Spin at Storage Rings

Most of the current physics interest in polarized electron beams involves the use of *longitudinally* polarized beams. This has lead to the development of several

schemes to install spin rotation systems in storage rings.[14] These devices usually consist of several bending magnets that are installed in an experimental straight section. Both vertical and horizontal bend magnets are required to perform the spin rotation. After the interaction point, a mirror rotation must be performed to restore the vertical polarization before the beam enters the next machine arc. The designer of such a system faces a number of problems:

1. Depolarization will result from the vertical bending magnets (due to spin flip photon emission).
2. The spin rotation and anti-rotation must be precisely matched to avoid depolarizing the system.
3. The bending magnets produce synchrotron radiation which can interfere with the experiment.
4. The bend magnets introduce dispersion into the beam optics just before the interaction point.

A scheme which solves all of the above problems is a non-trivial undertaking. At this time, no spin rotation scheme has yet been implemented. However, there are plans to do so at the HERA electron-protron collider and several schemes are under study for the LEP electron-positron collider.

4. Polarimetry

The degree of polarization obtained from most electron sources often depends upon details of the source construction that the experimenter cannot control. The polarization of the beam from a given source can also vary in time. Depolarization effects can be caused by the acceleration and transport systems. It is therefore essential to be able to measure the polarization of an electron or positron beam.

How are such measurements made? A polarized electron bunch has no macro-

scopic properties that could be useful.* We are inevitably lead to consider microscopic processes, *i.e.*, spin-dependent scattering processes. The simplest such processes are the elastic processes. These have a number of very useful properties:

1. The cross sections for elastic scattering are normally quite large.
2. Elastic scattering processes have simple kinematical properties.
3. The physics of elastic electron (positron) scattering is quite well understood.

The most easily provided targets for an electron (or positron) beam are the most mundane ones: nuclei, electrons, and photons. All are currently being used to analyze the polarization of electron beams. This chapter is divided into three sections, one for each target type:

1. e^--nucleus scattering - also called Mott Scattering
2. $e^\pm$-electron scattering - also called Møller (Bhabha) Scattering
3. $e^\pm$-photon scattering - also called Compton Scattering

There are other techniques that have been used to measure the polarization of electron (positron) beams. These exceptions to the elastic scattering rule do have potential for use in some situations but are not currently being pursued in high energy work. One technique is to analyze the polarization of photons emitted in the bremsstrahlung process. Another is to examine the rate of two photon annihilation produced when a polarized positron beam strikes a polarized target.†

⋆ A polarized electron bunch is a *very* weak magnetic dipole. Unfortunately its strength is roughly seven orders of magnitude less than a piece of magnetized iron of comparable size.

† This technique is useful only at rather low positron energies.

4.1. MOTT SCATTERING

The scattering of relativistic electrons by nuclei was first considered by Mott in the late 1920's.[15] He discovered that, due to the coupling of the electron spin to its orbital motion, the cross section for the transversely polarized electrons has a right-left asymmetry.‡ The cross section can be written as

$$\frac{d\sigma}{d\Omega} = \left(\frac{d\sigma}{d\Omega}\right)_{unpol}\left[1 + S(\theta)\vec{P}\cdot\hat{n}\right] \tag{4.1}$$

where the unpolarized cross section is

$$\left(\frac{d\sigma}{d\Omega}\right)_{unpol} = \frac{Z^2e^4}{4m^2\beta^4c^4\sin^4(\theta/2)}\left[1-\beta^2\sin^2(\theta/2)\right](1-\beta^2) \tag{4.2}$$

and where $S(\theta)$ is an asymmetry function (now called the Sherman function) and $\hat{n}$ is the axial vector that is normal to the scattering plane, $\hat{n} = \vec{p}\times\vec{p}\,'/|\vec{p}\times\vec{p}\,'|$. Note that $\hat{n}$ has different signs for right-scattered electrons and left-scattered electrons. As advertised, the cross section is larger for right-scattered particles. Mott was able to calculate the asymmetry function for $\theta = 90°$,

$$S^2(90°) = \left(\frac{Z}{137}\right)^2\frac{\beta^2(1-\beta^2)}{2-\beta^2}. \tag{4.3}$$

Equation (4.3) manifests many of the properties of a complete calculation of $S(\theta)$. The results of a more complete calculation are shown in Figure 5. We can conclude the following:

1. The asymmetry function becomes zero as $\beta \to 0$ and as $\beta \to 1$. It is typically maximum in the region $\beta = 0.6 \to 0.8$.

2. The asymmetry function increases with increasing Z. Heavy nuclei are favored for polarization analysis.

‡ The sign of the effect is most easily seen by considering the coupling of the electron magnetic moment to the magnetic field generated by the nucleus in the rest frame of the electron.

3. The asymmetry function is largest near $\theta = 120°$, in the backward hemisphere.

Since $S(\theta)$ is large for low energy electrons (kinetic energies in the range 100 KeV to 300 KeV), it is most useful for studying the polarization of electron sources. A schematic of a hypothetical Mott polarimeter is shown in Figure 6. The electrons from a longitudinally polarized source are electrostatically deflected by 90°. Since the energy is very low, this has the effect of rotating the beam direction but not its polarization vector. The now transversely polarized electrons are then scattered from a gold foil. Gold has the virtue that it is a high Z material and can be made into very thin targets. The scattered electrons are detected in two electron detectors that are placed symmetrically about the beam axis at $\theta = 120°$. The counting rates in the right and left detectors, N_L and N_R, are related to the beam polarization by the expression,

$$P = \frac{1}{S(\theta)}\left(\frac{N_R - N_L}{N_R + N_L}\right). \tag{4.4}$$

We note that the analyzing power of the polarimeter is given by $S(\theta)$. For 100 KeV electrons that are incident upon gold nuclei, $S(120°) \simeq 0.4$.

Systematics

Since the Mott scattering cross section is quite large, polarization measurements are nearly always limited by systematic uncertainties. The following is a discussion of some of the problems.

Equation (4.4) leads to an immediate concern about how well the asymmetry function is known. It has been calculated to a precision of about 1% for several nuclei.[17] The asymmetry function has also been measured (although not to very high precision). The measurements make use of the fact that an unpolarized electron beam acquires a transverse polarization from Mott Scattering that is equal to $S(\theta)$ (this is obvious if one considers an unpolarized beam to be composed of two oppositely polarized beams of equal intensity). Therefore, if one performs

a *double* scattering experiment by requiring two coplanar scatterings of θ_1 and θ_2 degrees, an asymmetry $\delta = S(\theta_1)S(\theta_2)$ will be measured. All such measurements have confirmed the more precise calculations.

Systematic errors that arise from left-right differences in the spectrometer are normally easy to measure and correct. This can be done by reversing the source polarization (if possible) and by using targets of a low Z material (for which the asymmetry is small).

The most serious systematic errors that arise in Mott polarimeters come from multiple and plural scattering.* Low energy electrons can scatter by substantial angles in even the thinnest foil targets. Since the asymmetry function has a strong angular dependence, the effective function $S(\theta)$ for a given foil can differ substantially from the theoretical value. The normal technique is to measure P with targets of several thicknesses and extrapolate the result to zero thickness. With care, one can measure the absolute polarization of a given source to about 5% with this technique.

Archeology

An interesting but obscure experiment was performed by R.T. Cox, C.G. McIlwraith, and B. Kurrelmeyer in 1928.[18] They knew that electrons could be described by waves that are analogous to light waves. They also knew that electrons have two spin states. The obvious question was, *are the two spin states analogous to the two transverse polarization states of light*? They decided to try a double scattering experiment with electrons that was the analog of one done with x-rays.

Their apparatus is shown in Figure 7. It consisted of two coaxial solid cylinders which could be rotated about a hollow tubular axis. Horizontal tubes were drilled into both the upper and the lower cylinders. A radium source was installed in the upper horizontal tube. It produced electrons that were scattered

* The term plural scattering is used to refer to the case in which the electron suffers a few large angle scatterings.

downward from a gold target mounted at the top of the vertical tube. A second gold target scattered the beam into the lower horizontal tube. The electrons were detected in a spark gap located at the end of the second tube. They observed a significant right-left asymmetry in the plane that was normal to the source tube! *The asymmetry was produced from a completely symmetrical arrangement of the detector.* The reader is reminded that double Mott scattering produces an asymmetry that is maximal when the two scatterings are coplanar. It produces no effect when the scattering planes are orthogonal. The source of the asymmetry was, of course, the source. The electrons from a beta source are longitudinally polarized. The effect of the first scattering was to change the electron direction by 90°. The spin vector, unchanged by the first scattering, was therefore normal to the plane of the second scattering. The observed right-left asymmetry was due to the Mott scattering process that we've just discussed.

Cox et al. performed the experiment a year or so before Mott published his theory. They did, however, understand that the electron spin had to be normal to the second scattering plane to explain the result. Instead, they presumed that the transverse polarization of the emitted beam was somehow becoming exchanged with the incident beam direction during the first scattering. It was recognized at the time that their result violated parity. Unfortunately, their follow-up experiments were somewhat inconclusive and there was considerable bias in favor of parity conservation. Nevertheless, parity violation was observed in 1928, nearly thirty years before it was appreciated.

4.2. MØLLER (BHABHA) SCATTERING

It is clear that the spin-orbit interaction can cause appreciable effects only at *low* energies. Since the electromagnetic interaction conserves parity, we have little choice but to provide a polarized target for our electron or positron beam. The most easily provided polarized target consists of magnetized iron. At magnetic saturation, 2 of the 26 valence electrons of each atom align their magnetic

moments with the macroscopic field (their spins are anti-aligned). We are therefore interested in considering polarized electron-electron (Møller) scattering and polarized positron-electron (Bhabha) scattering.

The Feynman diagrams for both processes are shown in Figure 8. In lowest order, both processes proceed via two subprocesses. Bhabha scattering involves a t-channel photon exchange and an s-channel intermediate photon state. The lowest order Møller scattering diagrams are a t-channel exchange and a u-channel exchange. It is required by Fermi-Dirac statistics that the relative phase between the two subprocesses of both Bhabha scattering and Møller scattering is negative.* This has important consequences in the spin dependence of both cross sections.

For Bhabha scattering, the t-channel exchange contributes to the cross section both when the electron and positron spins are parallel (the spin 1 state) and when they are antiparallel (the spin 0 state). The s-channel diagram vanishes for the antiparallel spin configuration (because the electromagnetic current is a vector current). Because of the negative relative phase, *the cross section is larger for the antiparallel (spin 0) configuration.* This result is counter-intuitive to those accustomed to s-channel electron-positron physics.

For Møller scattering, both diagrams contribute to both spin configurations. The relative phase of the two diagrams insures the correct exchange asymmetry of the wave function. Note that when the incident spins are antiparallel, the scattered spins are also antiparallel. The antiparallel spin state contains an additional negative phase between the two possible orientations of the outgoing spins. The result is that the amplitudes add and the cross section is again larger for the antiparallel spin configuration.

The preceding arguments assume that all particles in the center-of-mass frame are sufficiently relativistic that we can ignore the mass effects. This happens for beam energies larger than several MeV. In the high energy limit and to lowest

---

$\star$ The relative phase angle between the amplitudes of the two subprocesses is π.

order, we can write the cross sections for Møller and Bhabha scattering in the cm frame as

$$\left(\frac{d\sigma}{d\Omega}\right)_{Moller} = \frac{\alpha^2}{s}\frac{(3+\cos^2\theta)^2}{\sin^4\theta}\left\{1 - P_z^1 P_z^2 A_z(\theta) - P_t^1 P_t^2 A_t(\theta)\cos(2\phi - \phi_1 - \phi_2)\right\} \tag{4.5}$$

$$\left(\frac{d\sigma}{d\Omega}\right)_{Bhabha} = \frac{\alpha^2}{4s}\frac{(3+\cos^2\theta)^2}{(1-\cos\theta)^2}\left\{1 - P_z^1 P_z^2 A_z(\theta) - P_t^1 P_t^2 A_t(\theta)\cos(2\phi - \phi_1 - \phi_2)\right\} \tag{4.6}$$

where: θ is the cm frame scattering angle; ϕ is the azimuth of the scattered electron (the definition of $\phi = 0$ is arbitrary); P_z^1, P_z^2 are the longitudinal polarizations of the beam and target, respectively; P_t^1, P_t^2 are the transverse polarizations of the beam and target, respectively; ϕ_1, ϕ_2 are the azimuths of the transverse polarization vectors; and $A_z(\theta)$ and $A_t(\theta)$ are the longitudinal and transverse asymmetry functions which are defined as

$$\begin{aligned} A_z(\theta) &= \frac{(7+\cos^2\theta)\sin^2\theta}{(3+\cos^2\theta)^2} \\ A_t(\theta) &= \frac{\sin^4\theta}{(3+\cos^2\theta)^2.} \end{aligned} \tag{4.7}$$

Both cross sections have the form of an unpolarized cross section multiplied by the sum of one and a polarization dependent term. In fact, it is the *same* polarization dependent term. This polarization dependent part is odd in either the beam or target polarizations. Therefore, if we form an asymmetry by reversing the sign of one of the polarizations, we get that

$$A_{ee} \equiv \frac{\sigma(P^1P^2) - \sigma(-P^1P^2)}{\sigma(P^1P^2) + \sigma(-P^1P^2)} = -P_z^1 P_z^2 A_z(\theta) - P_t^1 P_t^2 A_t(\theta)\cos(2\phi - \phi_1 - \phi_2). \tag{4.8}$$

The experimental polarization asymmetry is given by the product of $A_z(\theta)$, $A_t(\theta)$ and the beam and target polarizations.

We note that unpolarized cross sections for the two processes are quite different, as one would expect. It is therefore a bit surprising that the polarization

asymmetries are identical. The unpolarized cross sections and the longitudinal and transverse asymmetry functions are plotted as a function of $\cos\theta$ in Figure 9. Both cross sections peak in the forward direction due to the t-channel subprocess. The Møller cross section involves the scattering of identical particles and is therefore symmetric about $\cos\theta = 0$. Since they apply to the polarized Møller cross section, the longitudinal and transverse asymmetry functions have the same symmetry. In fact, both asymmetry functions are maximal at $\cos\theta = 0$. The longitudinal asymmetry at this angle is $7/9$ and the transverse asymmetry is $1/9$. The optimal angle for polarimetry is the one that maximizes the analyzing power. The analyzing power is proportional to the product of the unpolarized cross section and the square of the asymmetry. For longitudinal polarization analysis, the analyzing power is also maximal at $\theta = 90°$.

We should not be surprised that the asymmetry functions become small in the forward direction. They depend upon the relative size of the two subprocesses of each scattering process. As the magnitudes of the two diagrams become more equal, the asymmetries become larger. Since t-channel diagrams dominate both processes in the forward direction, the asymmetries must become small there.

Polarized Targets

Equation (4.8) forms the basis of a polarization measurement. One need only measure the experimental asymmetry A_{ee}, calculate the value[s] of $A_z(\theta)$ [or $A_t(\theta)$], and know the target polarization. Wait a moment, *know the target polarization*? It would be extremely dangerous to assume that an iron target was magnetically saturated to the theoretical maximum. In practice, the degree of electron polarization within a piece of iron depends upon:

1. The precise composition of the material.
2. The procedure by which the material is prepared. It is critically important that the material be annealed. Any mishandling can cause work hardening and destroy the magnetic properties.

3. The magnitude of the saturating field.

4. The shape of the target (the effect of edges can be very large).

The only practical method of understanding these effects is to measure the magnetization density of the target and to extract the electron polarization from that number. A diagram of a polarized electron target is shown in Figure 10. A modest (100 gauss) magnetic field can be applied along any of the three axes of the device to magnetize one of several foil targets (of various thicknesses). Because the external field is rather weak, it is important that the length of each target be much larger than the width (the reader is reminded that the boundary conditions at the iron-air interface make it much easier to magnetize an iron needle along its axis than transverse to its axis). The magnetization density is measured placing a pickup coil about the middle of a target. As the applied field is reversed, the total magnetic field linked by the coil can be measured. This is composed of two components: the internal field of the iron (the $\vec{B}$ field), and the driving field just outside of the target (the $\vec{H}$ field). The target is then removed, leaving the pickup coil in place. The measurement is then repeated. This time, the $\vec{H}$ field both inside and outside the target is measured. Taking the difference of the measurements, one can extract the magnetization density $\vec{M}$ of the target

$$\vec{M} = \frac{1}{4\pi}(\vec{B} - \vec{H}). \tag{4.9}$$

The magnetic moment of an atom consists of an orbital part and and a spin related part. It is therefore necessary to correct the measured magnetization density to extract that part due to the electron spins. The relationship between the spin related magnetization, $\vec{M}_s$, and the measured magnetization is [19]

$$\vec{M}_s = \frac{2(g'-1)}{g'}\vec{M}, \quad g' = \frac{g}{g-1} \tag{4.10}$$

where g is the measured gyromagnetic ratio for the target material. For iron,

$g' \simeq 1.90$.[20] The polarization of the target is then given by the relationship

$$P_{tgt} = \frac{M_s}{N_e \mu_e} \tag{4.11}$$

where N_e is the electron density and μ_e is the electron magnetic moment. In practice, the measurement of P_{tgt} is limited by systematic effects to a few percent.

Kinematics of the $e^{\pm}$-e^{-} System

In the high energy limit, the laboratory frame variables are very simply related to the center-of-mass frame scattering angle. Let P and P' be the incident and scattered electron (positron) momenta in the laboratory frame. They are related the cm scattering angle, θ, by the expression

$$P' = \frac{P}{2}(1 + \cos\theta). \tag{4.12}$$

The scattered momentum ranges from zero to the full beam momentum. At $\theta = 90°$, the scattered momentum is $1/2$ of the beam momentum. The laboratory scattering angle θ_{lab} is related to the momentum variables by an equally simple equation (valid for small angles)

$$\theta_{lab}^2 = 2m\left[\frac{1}{P'} - \frac{1}{P}\right]. \tag{4.13}$$

This angle is normally quite small. At a beam energy of 47 GeV, the laboratory scattering angle that corresponds to a cm angle of 90° is 4.7 milliradians (0.27°).

Polarimetry

We have thus far sketched the ideas that a Møller or fixed target Bhabha polarimeter is based upon. We can measure the polarization along each of three axes by simply providing a magnetized target for each direction (although not simultaneously) and by measuring the asymmetry in the rate of electrons (positrons) scattered into a well defined solid angle. A scheme for doing this is

shown schematically in Figure 11. Note that the horizontal bending magnets have no function for the polarimeter (they make synchrotron radiation for the SLC energy spectrometer and background for the polarimeter). The main elements of the polarimeter are:

1. A magnetized foil target.
2. A collimator to define a scattering plane (defines the azimuth of the scattered particles).
3. A magnet and aperture that select the momentum range to be accepted (by Equation (4.12), this is equivalent to selecting the cm scattering angle). Note that the bending plane of the magnet is perpendicular to the scattering plane defined by the collimator. This is done to decouple P' from θ_{lab}.
4. A detector that is capable of measuring the electron rate as a function of position. Since the cross sections are fairly large, the detector must typically *count* many particles simultaneously (at SLC, the Møller polarimeters accept about 50 electrons/pulse).

Backgrounds

A magnetized foil target contains more than polarized electrons. It contains a substantial number of nuclei as well. Elastic electron (positron)-iron nucleus scattering produces no background to a well-designed polarimeter (the scattered electrons have the entire beam momentum whereas the Møller electrons have about half the beam momentum). Since the cross section for deeply inelastic scattering is very small as compared with the Møller and Bhabha cross sections, it also is not a serious source of background. Note, however, that the radiative elastic scattering process does have a large cross section and produces off-momentum electrons. The cross section for $e^{\pm} + N \rightarrow e^{\pm} + N + \gamma$ was first calculated by Bethe and Heitler[21] in 1934.* The exact size of this background

* Because most people are interested in the photon spectrum, their result is normally presented in a form that has had the scattered electron variables integrated away.

depends upon the polarimeter design but is in the range $10\% \rightarrow 20\%$. An electron signal that was measured in an actual Møller polarimeter is shown in Figure 12. The number of detected electrons is shown as a a function of scattering angle (the upper plot). There is a peak at the angle which corresponds to the accepted momentum. The background is well described by the Bethe-Heitler process. Note that this background is much more serious for a Bhabha polarimeter. The cross section for Bhabha scattering at $\theta_{cm} = 90°$ is smaller than the Møller scattering cross section by a factor of four. The signal-to-noise ratio is therefore decreased by the same factor.

Systematic Errors

The ability to operate a polarimeter in four polarization modes (two beam polarization directions $\times$ two target polarization directions), helps to study many possible systematic problems. Nevertheless, any polarization measurement will be limited by a number of possible systematic errors. The following is a partial list:

1. It is relatively straightforward to measure the target polarization to a precision of two or three percent. There is no conceptual reason why this could not be improved with a sufficiently well designed target.

2. The intrinsic background discussed in the last section must be subtracted. The resulting uncertainty can certainly be less than two percent (for Møller scattering).

3. A complete set of radiative corrections for polarized Møller and and Bhabha scattering has not been calculated. The effect on the size of the cross sections is quite large (of order 20%). The effect on the asymmetry is estimated to be quite small (less than 1%).

4. The measurement of an asymmetry is sensitive to the linearity of the detector. The non-linearities must be controlled to the one or two percent level.

5. The passage of the beam through the target can disrupt the spin alignment of the electrons. At SLC, the effect is estimated to be less than a one percent uncertainty on the target polarization. However, the problem could become severe at future linear colliders (actually this problem is a red herring since beam conditions that are extreme enough to depolarize a target are likely to destroy it).

Summary

Møller and Bhabha scattering can be used to perform three-axis polarimetry on non-recirculated beams of arbitrarily high energy. The analyzing power in the transverse directions is usually smaller than that for the longitudinal direction by a factor of $(1/7)^2 = 1/49$. Even for the longitudinal case, the measured asymmetry is small. At SLC, Equation (4.8) becomes

$$A_{ee} = \mathcal{P}_z^1 \mathcal{P}_z^2 A_z(90°) \simeq 0.4 \cdot 0.077 \cdot 7/9 = 2.4\%. \qquad (4.14)$$

The cross sections are quite large. At SLC, several tens of scattered electrons can be detected per machine pulse. And finally, the technique can provide moderate precision. Systematic uncertainties on the beam polarization of 5% have been achieved. It is possible that 2% could be achieved in the future.

4.3. Compton Scattering

Another easily provided, polarizable target for an electron or positron beam is a beam of photons. Electron (positron) - photon elastic scattering is normally called Compton scattering. Feynman diagrams of the two lowest order subprocesses are shown in Figure 13. The scattering process proceeds via s-channel and t-channel electron exchanges. The relative phase of the two diagrams is positive.* Both diagrams contribute to the scattering process when the incident spins are antiparallel (spin 1/2 case). However, when the spins are parallel (the spin 3/2

* The relative phase angle of the two amplitudes is zero.

case), the s-channel amplitude becomes zero. Therefore, the cross section is again larger for the antiparallel spin configuration.

Because optical photons have very little energy, the total energy in the center-of-mass frame is quite small. The collision of a 46 GeV electron with a photon of energy 2.23 eV (from a Nd:YAG laser) has a total center-of-mass energy (squared) of

$$s = m^2 + 4E_e E_\gamma \simeq (2.6 + 4.1) \times 10^{-7}\ \mathrm{GeV}^2 \tag{4.15}$$

where E_e and E_γ are the electron and photon energies, respectively. Note that the ratio m^2/s is not small. We cannot ignore mass terms in this frame. The center-of-mass frame therefore has no particular advantage for simplifying the form of the cross section. Making use of the idiom, *if you can't beat them, then you might as well join them*, we'll consider the differential cross section in the frame of maximal mass effects, the rest frame of the electron.

The differential cross section for the scattered photon in the rest frame of the electron is given by the expression [22]

$$\left(\frac{d\sigma}{d\Omega}\right)_{Compton} = \frac{1}{2} r_\circ^2 \left(\frac{k'}{k}\right)^2 \left[\frac{(k-k')^2}{kk'} + 1 + \cos^2\theta_\circ\right] \left\{1 - P^\gamma P^e A^{e\gamma}(\vec{k}, \vec{k}')\right\} \tag{4.16}$$

where: $r_\circ$ is the classical radius of the electron ($r_\circ = 2.82 \times 10^{-13}$ cm); $\vec{k}$ and $\vec{k}'$ are the momenta of the incident and scattered photons, respectively; $\theta_\circ$ is the photon scattering angle (the famous relationship between $\theta_\circ$ and k, k' is $1 - \cos\theta_\circ = m[1/k' - 1/k]$); P^γ is the circular polarization of the photon; P^e is the electron polarization; and the asymmetry function $A^{e\gamma}(\vec{k}, \vec{k}')$ is defined as

$$A^{e\gamma}(\vec{k}, \vec{k}') = \frac{\left(\frac{1}{k'} - \frac{1}{k}\right)\left[\vec{k}\cos\theta_\circ + \vec{k}'\right] \cdot \hat{s}}{\frac{(k-k')^2}{kk'} + 1 + \cos^2\theta_\circ} \tag{4.17}$$

We note that only photon helicity states couple to the electron polarization. (The scattering of *linearly* polarized photons by electrons produces an azimuthal

asymmetry that is independent of the electron spin.) The asymmetry function depends upon the scalar product of a linear combination of $\vec{k}$ and $\vec{k}'$ with the electron spin direction. In principle, this permits three axis polarimetry. In practice, however, such a device would be difficult to construct and operate.

Compton Scattering Kinematics

The kinematical properties of the scattering of a high energy electron with an optical photon seem quite strange to those accustomed to working in reference frames that are nearer the center-of-mass frame. The energy of the electron is typically 10 orders of magnitude larger than that of the photon. It is clear that all final state particles are swept into the forward direction (along the incident electron direction). It is therefore convenient to define all angles with respect to the incident electron direction. The direction of the outgoing photon, θ_K, differs from the normal definition of the scattering angle by 180° (if the colliding e-γ are collinear). If we let E, E', K, and K' be the incident electron energy, scattered electron energy, incident photon energy, and scattered photon energy, we can write the maximum energy of the scattered photon K'_{max} and the minimum energy of the scattered electron E'_{min} as

$$\begin{aligned} K'_{max} &= E(1-y) \\ E'_{min} &= Ey \end{aligned} \tag{4.18}$$

where the parameter y is defined as

$$y \equiv \left(1 + \frac{4EK}{m^2}\right)^{-1}.$$

The emission angle of the scattered photon θ_K is related to the scattered photon energy by the following expression,

$$K' = K'_{max}\left[1 + y\left(\frac{E\theta_K}{m}\right)^2\right]^{-1} = K'_{max} \cdot x. \tag{4.19}$$

The parameter x varies from unity at zero emission angle to zero at larger angles. The scale of the angular range is set by the angle for which the energy has been

reduced by a factor of two. This occurs when $E\theta_K\sqrt{y}/m = 1$ or at the angle $\theta_K = m/E\sqrt{y}$. As an example, we'll assume that a 46 GeV electron collides with a photon from a frequency doubled Nd:YAG laser (the photon energy is 2.23 eV). The value of y in this case is 0.389 which implies that the maximum photon energy is 28.1 GeV and that the minimum electron energy is 17.9 GeV. The angle at which the photon energy has been decreased by a factor of two is 1.8×10^{-5} radians. We see that the high energy photons remain along the beam direction.

The Tranformation from the Electron Rest Frame to the Laboratory Frame

The transformation from the electron rest frame variables to the laboratory variables is given by the following equations:

$$\begin{aligned} K &= \frac{2E}{m}k \\ x &= \frac{K'}{K'_{max}} = \frac{1-\cos\theta_\circ}{2y+(1-y)(1-\cos\theta_\circ)}. \end{aligned} \tag{4.20}$$

Using Equations (4.20), we can express the Compton cross section as given in Equations (4.16) and (4.17) in terms of the laboratory variables x, y, and the azimuth of the photon with respect to the electron transverse polarization ϕ,[23]

$$\left(\frac{d^2\sigma}{dxd\phi}\right)_{Compton} = \left(\frac{d^2\sigma}{dxd\phi}\right)_{unpol}\left\{1 - P^\gamma\left[P_z^e A_z^{e\gamma}(x) + P_t^e \cos\phi A_t^{e\gamma}(x)\right]\right\} \tag{4.21}$$

where the unpolarized cross section is defined as

$$\left(\frac{d^2\sigma}{dxd\phi}\right)_{unpol} = r_\circ^2 y\left\{\frac{x^2(1-y)^2}{1-x(1-y)} + 1 + \left[\frac{1-x(1+y)}{1-x(1-y)}\right]^2\right\}$$

and where the longitudinal and transverse asymmetries are defined as

$$\begin{aligned} A_z^{e\gamma}(x) &= r_\circ^2 y[1-x(1+y)]\left\{1 - \frac{1}{[1-x(1-y)]^2}\right\}\cdot\left(\frac{d^2\sigma}{dxd\phi}\right)^{-1}_{unpol} \\ A_t^{e\gamma}(x) &= r_\circ^2 yx(1-y)\frac{[4xy(1-x)]^{1/2}}{1-x(1-y)}\cdot\left(\frac{d^2\sigma}{dxd\phi}\right)^{-1}_{unpol} \end{aligned}$$

These equations are difficult to visualize and interpret without a bit of assis-

tance. The unpolarized cross section and the longitudinal and transverse asymmetries are plotted as functions of x in Figure 14 for the case of a 2.33 eV photon incident upon a 46 GeV electron ($y = 0.389$). We note that the cross section is very large (several hundred millibarns) and peaked at $x = 1$. The longitudinal asymmetry has a maximum of 75% also at $x = 1$. Note, however, that as x is decreased, $A_z^{e\gamma}$ decreases rapidly and becomes negative near $x = 0.72$. It reaches a minimum of -25% near $x = 0.47$ and returns to zero at $x = 0$. The transverse asymmetry is zero at both endpoints and reaches a maximum of 33% near $x = 0.75$.

Compton Polarimetry

A greatly simplified diagram of a generic Compton Polarimeter is shown in Figure 15. The electron (positron) beam is brought into collision with a circularly polarized laser beam at a small angle.

The current laser of choice is the frequency doubled Nd:YAG laser which produces red photons of energy 2.23 eV. They are capable of producing short (less than 10 ns) pulses of several millijoules to several hundred millijoules. The repetition rate of these devices is normally in the range of ten to one hundred pulses per second. The rate of Compton scatters is typically 100 to 10,000 per pulse, depending upon the electron current. The linearly polarized laser light is converted to a circularly polarized beam by passing it through an electrically reversible birefringent cell known as a Pockel's cell. The voltage is adjusted to produce a 1/4 wave shift and can be reversed (reversing the polarization) each pulse. With care, the polarization of the photon beam can be nearly 100%.

The scattered electrons and photons travel with the unscattered electron beam until they are separated by a bending magnet. The photons, of course, continue to travel in the same direction. The trajectories of the scattered electrons are bent by larger angles than the unscattered beam. Normally, one detects either the photons or the scattered electrons. Attempting to detect electron photon coincidences would severely limit the rate which could be counted.

Detecting the electrons has a number of advantages and limitations. The largest analyzing power occurs at large x. This is where the electrons have the smallest energy and are easiest to separate from the beam. A simple position sensitive detector can easily measure the rate as a function of electron energy. This provides many systematic checks and allows for the direct measurement of background (the signal and background have very different energy spectra). Unfortunately, it is generally not possible to measure the transverse polarization of the incident beam by detecting the electrons. Referring to Equation (4.21), we note that the transverse asymmetry is modulated by the factor $\cos\phi$. Accepting electrons from the entire azimuth causes the transverse cross section to integrate to zero. It is necessary to split the azimuth into at least two parts to make a transverse measurement. We have seen that the laboratory scattering angle of the electrons (which is similar to the emission angle of the photons) is very small (tens of microradians). It is therefore necessary to have a very parallel incident electron beam and to let the scattered electrons drift a large distance before any attempt is made to separate the beams. In any real accelerator, this is impossible. Quadrupoles are normally needed in straight sections.

Detecting the photons also has advantages and limitations. The energy spectrum of a photon flux is more difficult to measure than that of an electron flux. One can integrate the entire photon energy and measure the polarized energy asymmetry. This has the unfortunate result of severely reducing the analyzing power. The advantage of photon detection is that it permits transverse polarimetry. As we have seen, storage rings develop vertical polarization. The coupling of the electron polarization to the photon helicity produces an up-down asymmetry in the scattered particles. A detector placed above and/or below the beam plane can measure the transverse polarization. This also avoids the intense synchrotron radiation present in the beam plane. Note that averaging over azimuth effectively reduces the working asymmetry from more than 30% to less than 15%.

Backgrounds

Unlike the Møller technique, Compton scattering doesn't have an intrinsic background problem but machine-related backgrounds are quite common. Since nearly all Compton polarimeters are near an electron-positron collision point, radiative Bhabha scattering usually provides a significant background of off-energy electrons and photons. These depend very much on the particulars of the polarimeter and the machine. However, background levels of a few percent to ten percent are typical for a well-designed system. Such backgrounds can, of course, be measured (by not firing the laser).

Radiative Corrections

A complete set of first order radiative corrections to polarized Compton scattering has been calculated by Gongora and Stuart.[24] The effect on the tree level cross section is to change it by less than three percent. The effect on the asymmetries is less than one precent.

Systematic Uncertainties

The kinds of systematic uncertainty that affect a Compton scattering based polarization measurement are very similar to those that apply to Møller scattering. The following is a short list:

1. As with Møller scattering, it is essential to understand the degree of polarization of the target. Normally, the laser beam must be passed through windows and reflected from mirrors. This can easily cause depolarization and must be done very carefully. It appears that the uncertainty on the beam polarization can be controlled to $\Delta P^{\gamma}/P^{\gamma} \lesssim 1\%$.

2. As was mentioned previously, there is no intrinsic background to Compton scattering. Most Compton polarimeters must deal with machine backgrounds. The rate of such backgrounds can easily be measured with sufficient precision to reduce their effect upon polarization measurement to less than a few tenths of a percent.

3. As with the Møller case, it is essential to monitor non-linearities of the detection system. Most detection systems are not linear to better than a percent or several percent. These must be corrected to a level that is compatible with the other uncertainties.

4. Since the longitudinal asymmetry is a strong function of the scattered particle momentum, it is very important to understand the energy scale of the detector. If we take the case of a 46 GeV electron incident upon a 2.33 eV photon, an energy shift of 100 MeV causes a fractional change in the asymmetry of 1.1 %. The transverse asymmetry has a much smaller energy dependence about the maximum and this effect becomes negligible.

Bottom Line

The Compton scattering technique has several advantages and several disadvantages as compared with the Møller technique. The advantages are:

1. The target polarization of a Compton polarimeter is 13 times larger than that of a Møller polarimeter. The measured asymmetry is larger by roughly the same factor (because the theoretical asymmetries are comparable). The number of events needed to measure the beam polarization to a given precision scales with the square of the measured asymmetry. Therefore, a given Møller measurement requires a sample of data that is more than 100 times larger than a comparable Compton measurement.

2. The systematic error in the degree of target polarization is probably smaller for a Compton polarimeter.

3. The Compton process does not have an intrinsic background problem.

4. Compton devices are non-destructive to circulating beams and can be used at storage rings.

The disadvantages of the Compton process are:

1. All Compton polarimeters built thus far are single axis devices. A two axis device is conceptually possible but would be non-optimal. (This is

obvious if one compares the longitudinal and transverse asymmetries as shown in Figure 14. The maxima of the asymmetries tend to occur at the zero points of the other asymmetry.) Three axis Møller polarimeters are relatively straightforward to build and operate.

2. The longitudinal polarization asymmetry of Compton scattering is a strong function of the scattered particle energy. Very good detector resolution and calibration are required. The dependence of the longitudinal Møller asymmetry upon the scattered particle energy is much weaker. The requirements upon the detection system can be relaxed considerably.

3. The laser targets used in Compton scattering are complex and expensive devices as compared to the foil targets used for Møller scattering.

5. The Polarized SLC

Considerable is being made to polarize the electron beam of the SLAC Linear Collider. The machine is shown schematically in Figure 16. A gallium arsenide based photon emission source produces pulses of up to 10^{11} longitudinally polarized electrons at repetition rates of up to 180 Hz. The electrons are then accelerated in the first sector of the linac. The beam pulse achieves an energy of 1.21 GeV as it arrives at the entrance of the LTR (Linac To Ring) transfer line.

The electrons must be stored in the North Damping Ring for one machine cycle (the cycle time is ≥ 5.5 ms). As we have already seen, only vertical polarization can be maintained in a storage ring. It is therefore necessary to rotate the spins into the vertical direction. The angle of the initial LTR bend has been chosen to precess the spins of 1.21 GeV electrons by $5 \times 90°$ (requires a bending angle of $5 \times 32.8°$). The electron spins are therefore rotated into the horizontal direction. A superconducting solenoid (of strength 6.34 Tm) is then used to rotate the spins into the vertical direction and the bunch is stored in the damping ring. After one machine cycle, the bunch is extracted and passed through another

superconducting solenoid of the same strength. The spins are rotated back into the horizontal plane. The bend angle of the RTL (Ring To Linac) transfer line has been chosen to precess the spins by $3 \times 90°$. The beam pulse arrives back in the linac with its original longitudinal polarization. It is necessary, in general, to accelerate beams of arbitrary spin direction in the linac. The addition of a third superconducting solenoid into sector 2 of the linac, downstream of the RTL-linac interface, provides sufficient flexibility to do this (it must be used in combination with the RTL optics).

The beam pulse is then accelerated to nearly 50 GeV in the linac. To insure that the spin gymnastics in the damping ring have worked properly and to study many of the potential sources of depolarization, a Møller polarimeter is located at the end of the linac near the PEP injection line. This polarimeter is used primarily for diagnostic purposes.

The beam pulse is then transported through the north machine arc and the final focus section to the interaction point. At full energy, the spin vectors precess roughly 26 times. Since the arcs are not planar, vertical precession also occurs. Since longitudinal polarization is required at the interaction point, the precession must be calculated for the exact machine energy and the polarization at the arc entrance appropriately adjusted.

After colliding with the unpolarized positron bunch, the electron beam is transported through the south final focus system where a Compton polarimeter is located. The beam continues to the south extraction line where a second Møller polarimeter is located. The bending magnets of the final focus and extraction line cause an additional spin precession of roughly 540° between the interaction point and the Møller target. Both polarimeters continuously monitor the beam polarization.

LECTURE II: POLARIZED ELECTRON-POSITRON PHYSICS

In the first lecture, we discussed some of the techniques that are currently being used to produce, transport, and monitor polarized electron and positron beams. This lecture will survey some of the physical applications to which such beams can be put. As was discussed in the introduction to the first lecture, electron-positron colliders have now achieved sufficient energy that the weak interactions can be observed directly. The Z° pole represents the beginning of this energy regime. The pole is a rich source of information about the Standard Model and its range of validity. For the purposes of this lecture, we therefore choose to redefine the title of this Institute to *Looking At and Beyond The Z°*.

6. Definitions

It is convenient, for the purposes of this lecture, to slightly change the coordinate system convention that we have been using. The momentum variables are still described by a right-handed coordinate system. The incident electron direction defines the z-axis. The y-axis points vertically upward and the x-axis is horizontal. However, the longitudinal polarizations of the electron and positron beams will be described in terms of a helicity basis rather than in terms of a spatial coordinate system. Right-handed particles have $P_z = +1$ and left-handed particles have $P_z = -1$. The transverse polarizations will still be described in terms of the spatial coordinate system. These conventions are shown in Figure 17.

7. The Cross Section for $e^+e^- \rightarrow f\bar{f}$

The dominant electron-positron annihilation cross sections at energies that are comparable to or less than the threshold for W boson pair production are those that produce fermion-antifermion ($f\bar{f}$) pairs. It is quite instructive to study the polarization dependence of the $f\bar{f}$ cross section.

Let us assume that the matrix elements for annihilation of a left-handed electron with a left-handed positron and a right-handed electron with a right-handed positron are zero (vector and axial vector currents have this property). The matrix element for the process $e^+e^- \rightarrow f\bar{f}$ is then given by the following expression,

$$\sum_{\substack{\text{final}\\ \text{spins}}} |\mathcal{M}|^2 \sim (1-\mathcal{P}_z^-)(1+\mathcal{P}_z^+)|\mathcal{M}_L|^2 + (1+\mathcal{P}_z^-)(1-\mathcal{P}_z^+)|\mathcal{M}_R|^2 + 2\mathcal{P}_t^-\mathcal{P}_t^+\left[\mathrm{Re}(\mathcal{M}_L\mathcal{M}_R^*)\cos\Phi + \mathrm{Im}(\mathcal{M}_L\mathcal{M}_R^*)\sin\Phi\right] \tag{7.1}$$

where: $\mathcal{P}_z^{\pm}$, $\mathcal{P}_t^{\pm}$ are the longitudinal and transverse polarizations of the positron and electron beams; $\mathcal{M}_L$ is the matrix element for annihilation of a left-handed electron with a right-handed positron; and $\mathcal{M}_R$ is the matrix element for the annihilation of a right-handed electron with a left-handed positron. The quantity Φ is defined by the expression

$$\Phi = 2\phi - \phi^- - \phi^+ \tag{7.2}$$

where ϕ is the azimuth of the outgoing fermion and $\phi^{\pm}$ is the azimuth of the positron(electron) transverse polarization vector.

Using Equation (7.1), we can write the cross section for $e^+e^- \rightarrow f\bar{f}$ in the center-of-mass frame as[25]

$$\frac{4s}{\alpha^2}\frac{d\sigma}{d\Omega} = (1-\mathcal{P}_z^+\mathcal{P}_z^-)\sigma_u + (\mathcal{P}_z^+ - \mathcal{P}_z^-)\sigma_z + \mathcal{P}_t^+\mathcal{P}_t^-\left[\sigma_t\cos\Phi + \tilde{\sigma}_t\sin\Phi\right] \tag{7.3}$$

where s is the square of the center-of-mass frame energy and where the various

helicity cross sections and their matrix element compositions are listed in Table II:

Table II

The Helicity Cross Sections for the Process $e^+e^- \to f\bar{f}$

Symbol	Helicity Cross Section	Matrix Element Structure
σ_u	Unpolarized	$\sigma_u \sim (\|\mathcal{M}_L\|^2 + \|\mathcal{M}_R\|^2)$
σ_z	Longitudinal	$\sigma_z \sim (\|\mathcal{M}_L\|^2 - \|\mathcal{M}_R\|^2)$
σ_t	Real Transverse	$\sigma_t \sim \mathrm{Re}(\mathcal{M}_L \mathcal{M}_R^*)$
$\tilde{\sigma}_t$	Imaginary Transverse	$\tilde{\sigma}_t \sim \mathrm{Im}(\mathcal{M}_L \mathcal{M}_R^*)$.

We note that the longitudinal cross section is non-zero whenever parity is violated (*i.e.*, whenever the left- and right-handed cross sections are different). The longitudinal polarization of either beam (or both beams) will cause the differential cross section to manifest σ_z. Transverse polarization effects are only possible if *both* beams are polarized.*

Let us assume that the process $e^+e^- \to f\bar{f}$ is mediated by photon and Z° exchange only. Although the tree-level cross sections are substantially modified by real and virtual first order corrections, it is very useful to consider only the lowest order terms. We shall discuss the effect of radiative corrections in a later chapter. Each of the four helicity cross sections then contains a photon exchange term, a Z° exchange term, and a photon-Z° interference term.

In general, the helicity cross sections depend upon: v and a, the vector and axial vector couplings of the Z° to the electron; v_f and a_f, the vector and axial vector couplings of the Z° to the fermionic current; Q_f, the electric charge of the fermion (in units of e); $\Gamma(s)$, the normalized Z° propagator ($\Gamma(s) = s/[s - M_Z^2 + iM_Z\Gamma_Z]$); and c, the cosine of the polar angle of the outgoing fermion. We have

* Transverse polarization of a single beam leads to effects of order $m/\sqrt{s}$.

chosen the following definition for the vector and axial vector coupling constants,

$$\begin{aligned} v_f &= (I_3^f - 2Q_f \sin^2\theta_w)/\sin 2\theta_w \\ a_f &= -I_3^f/\sin 2\theta_w \end{aligned} \tag{7.4}$$

where I_3^f is the third component of fermion weak isospin and $\sin^2\theta_w$ is the well-known electroweak mixing parameter. The following section lists the tree-level terms of the four helicity cross sections.† The reader's indulgence is requested.

1. The unpolarized cross section can be decomposed as follows:

$$\sigma_u = \sigma_u^\gamma + \sigma_u^{\gamma Z} + \sigma_u^Z, \tag{7.5}$$

$$\begin{aligned} \sigma_u^\gamma &= Q_f^2(1+c^2) \\ \sigma_u^{\gamma Z} &= -2Q_f \mathrm{Re}\{\Gamma(s)\}\left[(1+c^2)vv_f + 2caa_f\right] \\ \sigma_u^Z &= |\Gamma(s)|^2\left[(1+c^2)(v^2+a^2)(v_f^2+a_f^2) + 8cvav_fa_f\right]. \end{aligned}$$

2. The longitudinal cross section can also be decomposed into three parts:

$$\sigma_z = \sigma_z^\gamma + \sigma_z^{\gamma Z} + \sigma_z^Z, \tag{7.6}$$

$$\begin{aligned} \sigma_z^\gamma &= 0 \\ \sigma_z^{\gamma Z} &= 2Q_f \mathrm{Re}\{\Gamma(s)\}\left[(1+c^2)av_f + 2cva_f\right] \\ \sigma_z^Z &= -|\Gamma(s)|^2\left[2(1+c^2)va(v_f^2+a_f^2) + 4c(v^2+a^2)v_fa_f\right]. \end{aligned}$$

3. The real transverse cross section can be decomposed as follows:

$$\sigma_t = \sigma_t^\gamma + \sigma_t^{\gamma Z} + \sigma_t^Z, \tag{7.7}$$

$$\begin{aligned} \sigma_t^\gamma &= Q_f^2(1-c^2) \\ \sigma_t^{\gamma Z} &= -2Q_f \mathrm{Re}\{\Gamma(s)\}(1-c^2)vv_f \\ \sigma_t^Z &= -|\Gamma(s)|^2(1-c^2)(v^2-a^2)(v_f^2+a_f^2). \end{aligned}$$

† It is assumed that the mass of the fermion m_f is small as compared with $\sqrt{s}$.

4. The imaginary transverse cross section can be decomposed as follows:

$$\tilde{\sigma}_t = \tilde{\sigma}_t^{\gamma} + \tilde{\sigma}_t^{\gamma Z} + \tilde{\sigma}_t^{Z}, \tag{7.8}$$

$$\begin{aligned}
\tilde{\sigma}_t^{\gamma} &= 0 \\
\tilde{\sigma}_t^{\gamma Z} &= 2\mathrm{Im}\{\Gamma(s)\}(1-c^2)av_f \\
\tilde{\sigma}_t^{Z} &= 0.
\end{aligned}$$

Most of our discussion will involve the remarkable properties of polarized Z° production. At the Z° pole, the various helicity cross sections can be simplified considerably. The pure photon exchange terms (denoted by σ^{γ}) are quite small as compared with the pure Z° exchange terms (denoted by σ^{Z}). Most of the electroweak interference terms (denoted by $\sigma^{\gamma Z}$) are proportional to the real part of the Z° propagator

$$\mathrm{Re}\{\Gamma(s)\} = \frac{s(s-M_Z^2)}{(s-M_Z^2)^2 + M_Z^2\Gamma_Z^2}$$

which vanishes at $s = M_Z^2$. The only electroweak interference term that doesn't vanish at the Z° pole is the one in the imaginary transverse cross section,

$$\tilde{\sigma}_t^{\gamma Z} \propto \mathrm{Im}\{\Gamma(M_Z^2)\} = \frac{\Gamma_Z}{M_Z} \simeq 4\%.$$

The imaginary part of the propagator is equal to the ratio of the Z° width to its mass. This term is therefore very small. The complete, polarization-dependent cross section for $e^+e^- \to f\bar{f}$ at the Z° pole can thus be written as

$$\begin{aligned}
\frac{d\sigma}{d\Omega} = \frac{\alpha^2}{4}\frac{s}{(s-M_Z^2)^2 + M_Z^2\Gamma_Z^2}\times \\
\Big\{(1-P_z^+P_z^-)\left[(1+c^2)(v^2+a^2)(v_f^2+a_f^2) + 8cvav_fa_f\right] \\
-(P_z^+ - P_z^-)\left[2(1+c^2)va(v_f^2+a_f^2) + 4c(v^2+a^2)v_fa_f\right] \\
+P_t^+P_t^-\cos\Phi(1-c^2)(v^2-a^2)(v_f^2+a_f^2)\Big\}.
\end{aligned} \tag{7.9}$$

The interpretation of this mess is aided by a brief discussion of coupling constants.

Coupling Constants

It is often quite convenient to transform the vector and axial vector coupling constants to a left- and right-handed helicity basis.* The definitions of the left- and right-handed couplings to the Z° current are

$$\begin{aligned} g_L^f &= v_f - a_f = (2I_3^f - 2Q_f \sin^2\theta_w)/\sin 2\theta_w \\ g_R^f &= v_f + a_f = -2Q_f \sin^2\theta_w/\sin 2\theta_w. \end{aligned} \tag{7.10}$$

To get a feeling for the magnitude of the couplings of the various fermions to the Z°, Equations (7.4) and (7.10) are evaluated in Table III for a complete quark and lepton generation.

Table III

The coupling constants of various fermions to the Z°. The value of $\sin^2\theta_w$ is assumed to be 0.230. All coupling constants are listed in units of $[\sin 2\theta_w]^{-1}$.

Fermion	a	v	g_L	g_R
Neutrino	-0.5	0.5	1.0	0
Charged Lepton	0.5	-0.04	-0.54	0.46
u Type Quark	-0.5	0.19	0.69	-0.31
d Type Quark	0.5	-0.35	-0.85	0.15

Note that the vector coupling for charged leptons is quite small (equivalently, we could say that $|g_L| \simeq |g_R|$). The consequences of this fact will be discussed in the next chapter on asymmetries.

* Technically this is a *chirality* basis and not a helicity basis. However, since we have assumed that all fermion masses are small, this distinction remains one of terminology rather than one of physics.

8. Asymmetries

At low energies, the differential cross section for the process $e^+e^- \rightarrow f\bar{f}$ is dominated by photon exchange. As a consequence, the cross section has a symmetrical angular distribution and no particular polarization dependence. Searching for asymmetries of the cross section was therefore a useful technique for searching for new physics. The differential cross section at the Z° is expected to have nearly symmetrical leptonic angular distributions and to be nearly symmetric in the beam helicity. The deviations from symmetry are sensitive functions of the weak mixing parameter, $\sin^2\theta_w$. Measurements of the various asymmetries are expected to provide sensitive tests of the Standard Model. They are also expected to be sensitive to the presence of new physical phenomena. In the following sections, we shall discuss several of these asymmetries.

8.1. The Unpolarized Forward-Backward Asymmetry

The unpolarized forward-backward asymmetry has been used for some time to search for electroweak interference effects. At the Z° pole, it still retains some utility. The forward-backward asymmetry for the process $e^+e^- \rightarrow f\bar{f}$, A_{FB}^f, is defined by the expression

$$A_{FB}^f(x) \equiv \frac{\int_0^x dc \frac{d\sigma}{dc} - \int_{-x}^0 dc \frac{d\sigma}{dc}}{\int_{-x}^x dc \frac{d\sigma}{dc}} \tag{8.1}$$

where x is an integration limit imposed by the acceptance of the detector. At the Z° pole, we can substitute Equation (7.9) into Equation (8.1). The resulting prediction of the Standard Model for A_{FB}^f is

$$\begin{aligned} A_{FB}^f(x) &= F(x) \cdot \frac{3ava_fv_f}{(a^2+v^2)(a_f^2+v_f^2)} \\ &= F(x) \cdot \frac{3}{4} \frac{(g_L^2 - g_R^2)(g_L^{f^2} - g_R^{f^2})}{(g_L^2 + g_R^2)(g_L^{f^2} + g_R^{f^2})} \end{aligned} \tag{8.2}$$

where the function $F(x)$ is

$$F(x) = \frac{4x}{3+x^2}. \tag{8.3}$$

Since $F(1) = 1$, we choose to define the symbol $A_{FB}^f(1) = A_{FB}^f$.

We can make several observations about the forward-backward asymmetry.

1. The forward-backward asymmetry depends upon the couplings of both the electron and fermion to the Z°.

2. Since the flavor of a hadron jet is difficult to tag, precision measurements of A_{FB}^f are inevitably made with muons (or perhaps with tau leptons).

3. The forward-backward asymmetry for lepton final states* is quite small. Assuming lepton universality, the asymmetry is

$$\begin{aligned} A_{FB}^l &= \frac{3a^2v^2}{(a^2+v^2)^2} \\ &\simeq 2\% \quad (\text{at } \sin^2\theta_w = 0.230). \end{aligned}$$

The small size is caused by the quadratic appearance of the leptonic vector coupling.

8.2. The Left-Right Polarization Asymmetry

The forward-backward asymmetry is designed to select those parts of the differential cross section that are odd under spatial reflection. It is therefore useful for studying parity violating components of the cross section. As we have already seen, the longitudinal helicity cross section also violates parity. It has a spatially symmetric part and a spatially antisymmetric part. We shall find it useful to select the spatially symmetric part.

---

* We note A_{FB}^l is sometimes called the leptonic charge asymmetry because the negative particles are found preferentially in the forward (electron) hemisphere.

The effect of the longitudinal helicity cross section σ_z on the differential cross section is odd in the difference $P_z^+ - P_z^-$. It is therefore useful to define a generalized beam polarization P_g that has the same property and a convenient normalization,

$$P_g \equiv \frac{P_z^+ - P_z^-}{1 - P_z^+ P_z^-}. \tag{8.4}$$

Note that P_g is positive whenever the electron beam is left-handed and/or the positron beam is right-handed. It is negative whenever the reverse is true. The generalized polarization becomes unity when either beam is completely polarized. At SLC, the positron beam will be unpolarized. The generalized polarization therefore has the simple form, $P_g = -P_z^-$.

The left-right asymmetry can now be defined by the following expression,

$$A_{LR}^f(x) = \frac{\int_{-x}^{x} dc \frac{d\sigma}{dc}(P_g = 1) - \int_{-x}^{x} dc \frac{d\sigma}{dc}(P_g = -1)}{\int_{-x}^{x} dc \frac{d\sigma}{dc}(P_g = 1) + \int_{-x}^{x} dc \frac{d\sigma}{dc}(P_g = -1)}. \tag{8.5}$$

We can use the tree-level cross section given by Equation (7.9) to evaluate the left-right asymmetry at the Z° pole. Before doing so, it is convenient to rewrite the differential cross section in terms of the generalized polarization. Ignoring the transverse polarization terms and the normalization details, we can express the cross section as

$$\begin{aligned} \frac{d\sigma}{dc} \propto (1 + c^2)\left[(v^2 + a^2)(v_f^2 + a_f^2) - P_g 2va(v_f^2 + a_f^2)\right] \\ + c\left[8vav_f a_f - P_g 4v_f a_f (v^2 + a^2)\right]. \end{aligned} \tag{8.6}$$

Substituting this expression into Equation (8.5), we can write that the tree-level expression for $A_{LR}^f(x)$ at the Z° pole is

$$A_{LR}^f(x) = \frac{-2va}{(v^2 + a^2)} = \frac{g_L^2 - g_R^2}{g_L^2 + g_R^2}. \tag{8.7}$$

This equation is full of surprises! First of all, it does not have any dependence upon the final state fermion couplings. It depends only upon the initial state

electron couplings. Nor does it depend upon the acceptance of our detector. The x dependence of the cross section integrals has cancelled from the ratio. Finally, we note that the asymmetry is linear in the electron vector coupling. This has the advantage that the left-right asymmetry is much larger than the leptonic forward-backward asymmetry. At $\sin^2\theta_w = 0.230$, the left-right asymmetry is 0.16 which is about eight times larger than A^l_{FB}.

One might ask just how general these results are. Does the inclusion of final state hadronic interactions spoil the result? What is the result of adding all final state fermions (except the electron final states)? The following section sketches an argument due to Lynn and Verzegnassi.[26]

The effect of final state interactions and fragmentation can be incorporated into Equation (8.6) by replacing the factors $(1 + c^2)$ and c with f dependent functions,

$$\begin{aligned} 1 + c^2 &\rightarrow \mathrm{Sym}(c, f) \\ c &\rightarrow \mathrm{Antisym}(c, f) \end{aligned} \tag{8.8}$$

where $\mathrm{Sym}(c, f)$ is a symmetric function of c and $\mathrm{Antisym}(c, f)$ is an antisymmetric function of c. We now form the left-right asymmetry of the total event sample (which is obtained by summing symmetric integrals for each fermion type),

$$\begin{aligned} A_{LR} &= \frac{\sum_f \left\{ \int_{-x_f}^{x_f} dc \frac{d\sigma}{dc}(\mathcal{P}_g = 1) - \int_{-x_f}^{x_f} dc \frac{d\sigma}{dc}(\mathcal{P}_g = -1) \right\}}{\sum_f \left\{ \int_{-x_f}^{x_f} dc \frac{d\sigma}{dc}(\mathcal{P}_g = 1) + \int_{-x_f}^{x_f} dc \frac{d\sigma}{dc}(\mathcal{P}_g = -1) \right\}} \\ &= \frac{-2va \sum_f \int_{-x_f}^{x_f} dc (v_f^2 + a_f^2) \mathrm{Sym}(c, f)}{(v^2 + a^2) \sum_f \int_{-x_f}^{x_f} dc (v_f^2 + a_f^2) \mathrm{Sym}(c, f)} \\ &= \frac{-2va}{v^2 + a^2} = \frac{g_L^2 - g_R^2}{g_L^2 + g_R^2}. \end{aligned} \tag{8.9}$$

Note that in spite of final state effects and the use of different integration limits for each fermion type, the form of asymmetry is unchanged. It is a remarkably

robust quantity. We can use the entire sample of hadronic Z° decays as well as the muon and tau lepton final states to measure A_{LR}. The electron final states must be excluded because we have excluded the t-channel processes from our analysis.

Sensitivity to $\sin^2\theta_w$

The left-right asymmetry has a very simple dependence on the electroweak mixing parameter $\sin^2\theta_w$,

$$A_{LR} = \frac{2(1-4\sin^2\theta_w)}{1+(1-4\sin^2\theta_w)^2}. \tag{8.10}$$

The asymmetry is a very sensitive function of $\sin^2\theta_w$. Small changes in $\sin^2\theta_w$ lead to very large changes in A_{LR},

$$\delta A_{LR} \simeq 8\delta\sin^2\theta_w.$$

In constrast, the leptonic forward-backward asymmetry is much less sensitive to $\sin^2\theta_w$. A comparision of A_{FB}^l and A_{LR} is shown in Figure 18 as a function of $\sin^2\theta_w$. The advantage of A_{LR} is particularly pronounced in the region near $\sin^2\theta_w = 0.25$.

The Experimental Asymmetry

In a real experiment, one never has completely polarized beams. This causes the measured asymmetry A_{LR}^{exp} to differ from the theoretical asymmetry. The relationship of A_{LR}^{exp} to A_{LR} is given by the expression

$$A_{LR}^{exp} = \frac{N_{ev}(\mathcal{P}_g) - N_{ev}(-\mathcal{P}_g)}{N_{ev}(\mathcal{P}_g) + N_{ev}(-\mathcal{P}_g)} = \mathcal{P}_g A_{LR} \tag{8.11}$$

where $N_{ev}(\mathcal{P}_g)$ is the rate of events measured with a beam polarization of $\mathcal{P}_g$. The size of the measured asymmetry is equal to the product of the theoretical

asymmetry and the generalized polarization.*

It is rather simple to derive the error on the theoretical asymmetry that is expected after N_{tot} events,

$$\Delta A_{LR} = \left[A_{LR}^2 \left(\frac{\Delta \mathcal{P}_g}{\mathcal{P}_g} \right)^2 + \frac{1}{\mathcal{P}_g^2} \frac{1}{N_{tot}} \right]^{1/2} \tag{8.12}$$

where we have assumed that $(\mathcal{P}_g A_{LR})^2 \ll 1$. The first term in the square brackets gives the error on the left-right asymmetry in the limit of large statistics. The fractional uncertainty on A_{LR} is limited by the fractional uncertainty of the beam polarization. The second term gives the statistical error. Note that the rate of convergence to the asymptotic limit is governed by the size of $\mathcal{P}_g$.

The expected uncertainty of a measurement of the right-left asymmetry is shown in Figure 19 as a function of the number of Z° events collected. The beam polarization is taken to be 45%. The Z° mass is assumed to be 92.5 GeV. The corresponding uncertainty on $\sin^2\theta_w$ and on M_Z is shown on the right-hand scales. The three branches of the A_{LR} curve refer to the precision of the polarization monitoring. From top to bottom, ΔA_{LR} is shown for $\Delta\mathcal{P}/\mathcal{P} =$ 5%, 3%, and 1%, respectively. A sample of 10^5 to 10^6 events is sufficient to saturate the asymptotic limit, depending upon the precision of the polarization monitoring. The expected uncertainty on $\sin^2\theta_w$ from a measurement of the leptonic forward-backward asymmetry is also shown. The beams are assumed to be unpolarized and the number of muonic decays is assumed to be given correctly by the Standard Model. We note that the measurement of A_{LR} outperforms the forward-backward measurement in all cases.

The current and proposed precision of several other measurements of the electroweak parameters is also summarized in Figure 19. Note that only the left-right asymmetry measurement will provide information that is as precise as the

* A more sophisticated scheme to extract A_{LR} from various event rates has been proposed for LEP.[27] In principle, this scheme measures the beam polarization and the spin 0 cross section in addition to the theoretical asymmetry. It places rather different requirements on the beam polarimetry than those discussed in this section.

Z° mass measurement. We shall see in the next chapter that several independent and precise measurements are necessary to properly test the Standard Model.

8.3. The Polarized Forward-Backward Asymmetry

It is clear that the left-right asymmetry enables the efficient and precise measurement of the couplings of the weak neutral current to the electron. The predictions of the Standard Model can be given close scrutiny by this technique. However, it is still important to measure the coupling of the Z° to all possible fermions. It is certainly straightforward to detect and measure muon and tau lepton final states. Heavy quark final states aren't too difficult if semileptonic decays are used for tagging. Good microvertex detectors and particle identification appear to be very useful for this purpose as well.

We recall that the unpolarized forward-backward asymmetry was sensitive to the final state fermion couplings. In fact, we can rewrite the expression for A_{FB}^f (Equation (8.2)) as

$$A_{FB}^f = \frac{3}{4} \cdot \frac{g_L^2 - g_R^2}{g_L^2 + g_R^2} \cdot \frac{g_L^{f^2} - g_R^{f^2}}{g_L^{f^2} + g_R^{f^2}} = \frac{3}{4} \cdot A_{LR} \cdot A_{LR}^f \tag{8.13}$$

where we have defined A_{LR}^f to be the combination of fermionic coupling constants that is equal to A_{LR} in the case that f denotes an electron. Table IV lists A_{LR}^f and A_{FB}^f for each type of detectable fermionic final state. It is assumed that $\sin^2\theta_w = 0.230$.

Table IV

Fermion	A_{LR}^f	A_{FB}^f
Charged Lepton	0.16	0.02
u Type Quark	0.67	0.08
d Type Quark	0.94	0.11

Note that the small size of A_{LR} reduces the potentially large size of the forward-backward asymmetry.

We are lead to an obvious question, *what happens to the forward-backward asymmetry when polarized beams are used?* Substituting Equation (8.6) into Equation (8.1) (with $x = 1$), we can derive the forward-backward asymmetry for a beam polarization $\mathcal{P}_g$,

$$A_{FB}^f(\mathcal{P}_g) = \frac{3}{4} \cdot \frac{\mathcal{P}_g + A_{LR}}{1 + \mathcal{P}_g A_{LR}} \cdot A_{LR}^f = \frac{3}{4} \cdot \mathcal{P}_{eff} \cdot A_{LR}^f. \tag{8.14}$$

We note that the factor A_{LR} in the unpolarized case (which is the *natural* electron polarization caused by the Z° couplings) has now been replaced by the factor

$$\mathcal{P}_{eff} = \frac{\mathcal{P}_g + A_{LR}}{1 + \mathcal{P}_g A_{LR}}.$$

Because $A_{LR} > 0$, the forward-backward asymmetry becomes much larger when left-handed beam ($\mathcal{P}_g > 0$) is used. For example, when $\sin^2\theta_w = 0.230$ and $\mathcal{P}_g = 0.40$, the forward-backward asymmetries are all increased by a factor of 3.3!

In practice, it is not desirable to operate a polarized electron-positron collider with only one helicity state. The study of other physical processes benefits by the use of both helicity states. Many polarimeters need both helicity states to function. Unfortunately, the effective beam polarization, $\mathcal{P}_{eff}$, becomes less than the beam polarization $\mathcal{P}_g$ when the right-handed helicity state is selected. We must pay a price in analyzing power. Can we do something more clever than study the *traditional* forward-backward asymmetries?

An Improved Forward-Backward Symmetry

The answer to the above question is yes. It is possible to define a combination of the forward-backward and left-right asymmetries that selects just the final state couplings and has a simple dependence upon the beam polarization. This

improved forward-backward asymmetry, $\tilde{A}^f_{FB}(\mathcal{P}_g)$, is defined as

$$\tilde{A}^f_{FB}(\mathcal{P}_g) \equiv \frac{\sigma^f_F(\mathcal{P}_g) - \sigma^f_F(-\mathcal{P}_g) - [\sigma^f_B(\mathcal{P}_g) - \sigma^f_B(-\mathcal{P}_g)]}{\sigma^f_F(\mathcal{P}_g) + \sigma^f_F(-\mathcal{P}_g) + \sigma^f_B(\mathcal{P}_g) + \sigma^f_B(-\mathcal{P}_g)} \tag{8.15}$$

where we have used the shorthand notation

$$\sigma^f_F(\mathcal{P}_g) = \int_0^1 dc \frac{d\sigma^f}{dc}(\mathcal{P}_g)$$

$$\sigma^f_B(\mathcal{P}_g) = \int_{-1}^0 dc \frac{d\sigma^f}{dc}(\mathcal{P}_g).$$

Substituting Equation (8.6) into Equation (8.15), we derive the following tree-level expression for the improved forward-backward asymmetry

$$\tilde{A}^f_{FB}(\mathcal{P}_g) = \frac{3}{4} \cdot \mathcal{P}_g \cdot \frac{g_L^{f^2} - g_R^{f^2}}{g_L^{f^2} + g_R^{f^2}} = \frac{3}{4} \cdot \mathcal{P}_g \cdot A^f_{LR}. \tag{8.16}$$

As advertised, the improved forward-backward asymmetry, depends only upon the final state couplings. Comparing Equation (8.16) with Equation (8.14), we see that the factor $\mathcal{P}_{eff}$ has been replaced with the beam polarization $\mathcal{P}_g$. The magnitude of our improved asymmetry is therefore between the simple polarized forward-backward asymmetry with left-handed beam and that with right-handed beam. There is no particular statistical advantage in using it. It is sometimes claimed that the absence of A_{LR} from Equation (8.16) implies that A^f_{LR} can be measured with a smaller error. Actually, this may not be the case. If we assume that the statistical error is small as compared with the beam polarization uncertainty, the uncertainty on A^f_{LR} from a measurement of $\tilde{A}^f_{FB}$ is given by the following simple expression

$$\frac{\Delta A^f_{LR}}{A^f_{LR}} = \frac{\Delta \mathcal{P}_g}{\mathcal{P}_g}.$$

If we were to perform the same measurement with left-handed beam only, the error on A_{LR} is likely to be highly correlated with the polarization uncertainty.

If we assume that the polarization uncertainty dominates both quantities, then the uncertainty on A_{LR}^f is given by the following expression

$$\frac{\Delta A_{LR}^f}{A_{LR}^f} = \frac{\mathcal{P}_g - A_{LR}}{\mathcal{P}_g + A_{LR}}\left(\frac{\Delta \mathcal{P}_g}{\mathcal{P}_g}\right)$$
$$= 0.60\left(\frac{\Delta \mathcal{P}_g}{\mathcal{P}_g}\right) \text{ for } \mathcal{P}_g = 0.4,\ \sin^2\theta_w = 0.230.$$

We note that the experiment with left-handed beam has a systematic as well as an advantage in analyzing power. Of what advantage is the *improved* forward-backward asymmetry? We must discuss the effect of initial state radiative effects before drawing any conclusions.

The Effect of Initial State Radiation

It is well-known that initial state bremsstrahlung has an enormous effect on high energy electron-positron cross sections. The standard treatment of the problem involves describing the electron and positron with structure functions. The electron and positron are assumed to radiate the fractions $(1 - x^-)$ and $(1 - x^+)$ of their initial energies. It is assumed that all radiation is collinear with the beam directions. The square of the electron-positron center-of-mass energy, s, can therefore be written as

$$s = x^- x^+ s^\circ \tag{8.17}$$

where s° is the square of the nominal center-of-mass energy. The observed cross section σ_{obs} can then be written as a convolution of the tree-level cross section $\sigma_{tree}(s)$ and two structure functions,

$$\sigma_{obs} = \int dx^- dx^+ D(x^-, s^\circ) D(x^+, s^\circ) \sigma_{tree}(x^- x^+ s^\circ) \tag{8.18}$$

where the electron (positron) structure function $D(x, s)$ represents the probability that the particle retains a fraction x of its original momentum. Since the Z° pole is a strong resonance, we need concern ourselves only with relatively soft photon

emission (the total photon energy $E_\gamma \lesssim \Gamma_Z$). The structure function has been calculated by Nicosini and Trentadue[28] to be

$$D(x,s) \propto (1-x)^{\frac{\eta}{2}-1}$$
$$\eta = -6 \ln\left[1 - \frac{\alpha}{3\pi}\ln(s/m^2)\right]. \tag{8.19}$$

It is clear from Equation (8.18), that the sensitivity of an asymmetry to initial state radiative corrections depends upon the steepness of its variation with center-of-mass energy $\sqrt{s}$. The energy dependence of the various asymmetries (and many of the electroweak corrections) has been calculated by Blondel, Lynn, Renard, and Verzegnassi.[29] Their results are shown in Figure 20. The asymmetries $A_{FB}^f(\mathcal{P})$, $\tilde{A}_{FB}^f(\mathcal{P})$, and A_{LR} are shown as functions of $\sqrt{s^\circ}$ for several final state fermions. The unimproved forward-backward asymmetry is shown for the beam polarization $\mathcal{P}_g = 0.5,\ 0,$ and -0.5. The improved forward-backward asymmetry is shown for complete beam polarization. The unimproved forward-backward asymmetries are much more sensitive to $\sqrt{s}$ than are the improved varieties or the left-right asymmetry. This implies that initial state radiative corrections are significantly more important for the unimproved forward-backward asymmetries than they are for the other asymmetries. As a concrete example, a recent calculation by Kennedy, Lynn, and Im[30] finds that initial state radiative corrections alter the unpolarized forward-backward asymmetry for muons by 32%. The corresponding corrections to the left-right asymmetry shift it by less than 0.7%.

Technology with the Forward-Backward Asymmetry

The measurement of various forward-backward asymmetries will permit tests of lepton universality and measurements of the Z° coupling to the heavier quarks. Do they have any other utility?

Once the fermion forward-backward asymmetries have been measured, the answer is yes. A positive value for A_{FB} implies that the fermion moves preferentially along the electron direction and the antifermion along the positron

direction. For heavy quarks, this means that the jet direction can serve as a tag of baryon number. Normally, the semileptonic decays of heavy hadrons are required to tag the baryon number of a jet. For mixing and CP violation searches, this implies that two semileptonic decays are required. Since semileptonic branching ratios are typically about 10%, the efficiency of such techniques can be quite small. If A_{FB} for the process is reasonably large (like 30% or so), a considerable gain in efficiency can be had by using the forward-backward asymmetry and requiring only one semileptonic decay to tag baryon number. The application of this technique to b-quark CP violation is discussed in an accompanying document by P. Grosse-Wiesmann.[31]

8.4. The Transverse Asymmetries

As we discussed in the first lecture, storage rings naturally develop *transverse* beam polarization. A difficult and expensive spin rotation scheme is necessary to make longitudinally polarized beams. We should investigate then, what physical measurements can be made with transversely polarized beams.

The transverse asymmetries are defined as azimuthal moments of the cross section. They are defined to select the ratios of the real and imaginary transverse cross sections to the unpolarized cross section,

$$\begin{aligned} A_t^f &\equiv \frac{4}{P_t^+ P_t^-} \cdot \frac{\int d\Omega \cos 2\phi \frac{d\sigma}{d\Omega}}{\int d\Omega \frac{d\sigma}{d\Omega}} \\ \tilde{A}_t^f &\equiv \frac{4}{P_t^+ P_t^-} \cdot \frac{\int d\Omega \sin 2\phi \frac{d\sigma}{d\Omega}}{\int d\Omega \frac{d\sigma}{d\Omega}}. \end{aligned} \tag{8.20}$$

Substituting the tree-level cross section for $e^+e^- \to f\bar{f}$ (Equation (7.9)) into the above definitions, we can write that

$$\begin{aligned} A_t^f &= \frac{v^2 - a^2}{v^2 \mp a^2} = \frac{2g_L g_R}{g_L^2 + g_R^2} \\ \tilde{A}_t^f &= \frac{2av_f}{(v^2 + a^2)(v_f^2 + a_f^2)} \cdot \frac{\Gamma_Z}{M_Z}. \end{aligned} \tag{8.21}$$

The asymmetry A_t^f is, like A_{LR}, independent of the couplings to the final state fermions. It is quite large ($A_t \simeq -0.99$ at $\sin^2\theta_w = 0.230$) and it is relatively insensitive to $\sin^2\theta_w$. For small changes in $\sin^2\theta_w$, we can write that

$$\begin{aligned} \delta A_t &\simeq -16\ (1 - 4\sin^2\theta_w)\delta\sin^2\theta_w \\ &\simeq -1.28\ \delta\sin^2\theta_w \quad \text{at } \sin^2\theta_w = 0.230. \end{aligned} \tag{8.22}$$

Recall that the coefficient of $\delta\sin^2\theta_w$ was eight for the left-right asymmetry.

The asymmetry $\tilde{A}_t^f$ does have some sensitivity to the vector coupling of the final state fermions. Unfortunately, the asymmetry is fairly small (about 8% for u type quarks) and is therefore of limited utility.

9. Radiative Corrections

All of our discussion has thus far involved the use of tree-level expressions. We have shown that initial state radiative corrections make small changes in the tree-level expressions for the left-right and improved forward-backward asymmetries. However, we certainly cannot ignore the full spectrum of electroweak corrections. The interpretation of precise measurements will require that all corrections be included.

The Lagrangian of the Standard Model contains three parameters of direct relevance to Z° physics: the coupling constant of the SU(2) group of weak isospin, g; the coupling constant of the U(1) group of weak hypercharge, g'; and the vacuum expectation value of the Higgs field, $\langle\phi\rangle_\circ$. In order to specify the Standard Model precisely, it is necessary to provide three precisely measured physical quantities that are related to the three parameters.

At the current time, there are only two well-measured physical quantities. The first quantity is electric charge which has been measured by Thompson scattering with a fractional error of less than 3×10^{-8}. It is related to the

coupling constants by the expression

$$e^2 = 4\pi\alpha = \frac{g^2 g'^2}{g^2 + g'^2}. \tag{9.1}$$

The second quantity, the Fermi coupling constant G_F, has been been extracted from measurements of the muon lifetime. The fractional uncertainty is less than 2×10^{-6}. It is related to the vacuum expectation value of the Higgs field by the following expression

$$G_F = \frac{1}{\langle\phi\rangle_\circ^2 \sqrt{8}}. \tag{9.2}$$

It is expected that SLC and LEP will soon provide a precision measurement of a third necessary quantity, the Z° mass. At tree level, M_Z is related to the Standard Model parameters by the expression

$$M_Z^2 = \frac{(g^2 + g'^2)}{2} \cdot \langle\phi\rangle_\circ^2. \tag{9.3}$$

Unfortunately, the Z° mass is measured at a much higher energy scale than either α or G_F. The *running* of the electromagnetic coupling (due to photon vacuum polarization processes) is a large effect. It is useful, at this point, to introduce an auxiliary parameter, θ_w. At tree level, we can write that

$$\sin 2\theta_w = \frac{2gg'}{g^2 + g'^2} = \left[\frac{4\pi\alpha}{\sqrt{2} G_F M_Z^2}\right]^{\frac{1}{2}}. \tag{9.4}$$

The photon vacuum polarization effects can now be incorporated into the definition of θ_w. We shall follow the convention of Lynn, Peskin, and Stuart[32] by defining the weak mixing angle as follows,

$$\sin 2\theta_w = \left[\frac{4\pi\alpha}{\sqrt{2} G_F M_Z^2 (1 - 0.06)}\right]^{\frac{1}{2}}. \tag{9.5}$$

Note the presence of the term 0.06. It has the effect of removing the photon polarization corrections from any quantity that is expressed in terms of θ_w. These corrections are the largest ones that we shall make.

We note that a precision measurement of a fourth physical quantity (such as A_{LR} or the W boson mass) will **test** the Standard Model. Actually, there are at least two unknown parameters of the Standard Model that enter the electroweak corrections at the loop level: the top quark mass, m_t, and the the Higgs boson mass, m_H. A test that does not contradict the Standard Model would would merely place constraints on the masses.

A Word About Precision

The expected precision of an experimental measurement of the left-right asymmetry was given in Equation (8.12). Note that if the uncertainty is dominated by the statistical term, the error ΔA_{LR} is absolute (*i.e.*, it is independent of the size of A_{LR}). We should therefore compare the absolute size of the virtual corrections to the expected precision of the measurement. The reader is reminded that an uncertainty of $\Delta A_{LR} \simeq 0.01$ is possible at a polarized SLC with an event sample of roughly 60,000 Z° decays. If high precision monitoring of the beam polarization is achieved ($\Delta P/P \lesssim 1\%$), an ultimate error of $\Delta A_{LR} \simeq 0.002 \rightarrow 0.003$ is conceivable.

9.1. Standard Model Corrections to A_{LR}

The virtual corrections to the left-right asymmetry have been calculated on numerous occasions by a large community of people. Any attempt to give a proper account and accounting of all of the work would take several lectures and still be incomplete. The following is therefore a review of the content of only one publication [32] which this author regards as exceptional in its clarity and its completeness.

Several calculations of the left-right asymmetry are shown in Figure 21 as functions of the center-of-mass energy. The tree-level asymmetry is shown for Z° masses of 98 GeV, 94 GeV, and 90 GeV as a family of three dashed curves. The photon vacuum polarization correction is incorporated into A_{LR} by using Equation (9.5) to define $\sin^2\theta_w$. The corrected asymmetry is shown for the three

mass values by the dotted curves. The result of a complete first order treatment of all virtual corrections is shown as a solid curve for each mass value. The top quark and Higgs boson masses are assumed to be 30 GeV and 100 GeV, respectively. We note that the photon vacuum polarization correction is indeed the dominant correction. The theoretical uncertainty on the vacuum polarization correction has been analyzed by Lynn and Verzegnassi.[26] They find that the uncertainty on the asymmetry is $\Delta A_{LR} \lesssim 0.005$, due mostly to strong interaction uncertainties.

The result of the complete first order calculation for the left-right asymmetry at the Z° pole is summarized in Table V for several values of M_Z, m_t, and m_H. The asymmetry is very sensitive to large values of the top quark mass and is much less sensitive to the Higgs mass.

The sensitivity of the virtual corrections to the presence of a massive top quark is related to the symmetry of the SU(2) × U(1) Lagrangian. Because the Higgs fields form an SU(2) doublet, the Lagrangian possesses an additional global SU(2) symmetry. This additional symmetry is what causes the ρ parameter,

$$\rho \equiv \frac{M_W^2}{M_Z^2 \cos^2\theta_w}, \tag{9.6}$$

to be unity at tree level. The addition of isodoublets of particles with large mass splittings breaks the symmetry and causes the ρ parameter to deviate from one, $\rho \rightarrow 1 + \delta\rho$. Within our chosen renormalization scheme (*i.e.*, chosen definition of $\sin^2\theta_w$), it can be shown that small changes in ρ affect the left-right asymmetry as follows

$$\delta A_{LR} = \frac{64 \sin^4\theta_w \cos^2\theta_w}{\left[1 + (1 - 4\sin^2\theta_w)^2\right]^2} \delta\rho. \tag{9.7}$$

Therefore, the addition of isodoublets with large mass splittings also affects the left-right asymmetry.

The size of the effect on A_{LR} increases quadratically with the top quark mass

Table V

The result of a complete first order calculation[32] for the left-right asymmetry at the Z° pole. It is tabulated for several values of M_Z, m_t, and m_H.

$$A_{LR}(q^2 = -M_Z^2)$$

	M_Z	$m_H = 10$	$m_H = 100$	$m_H = 1000$
	90	.0613	.0536	.0423
	92	.1762	.1691	.1590
$m_t = 30$	94	.2756	.2692	.2602
	96	.3615	.3557	.3475
	98	.4354	.4302	.4229
	90	.0640	.0563	.0451
	92	.1786	.1716	.1615
$m_t = 60$	94	.2777	.2714	.2624
	96	.3633	.3575	.3495
	98	.4370	.4318	.4246
	90	.0703	.0626	.0513
	92	.1844	.1773	.1672
$m_t = 90$	94	.2830	.2767	.2676
	96	.3681	.3624	.3543
	98	.4414	.4362	.4290
	90	.0805	.0728	.0616
	92	.1936	.1866	.1765
$m_t = 130$	94	.2914	.2851	.2760
	96	.3757	.3699	.3619
	98	.4482	.4430	.4358
	90	.0975	.0898	.0786
	92	.2087	.2018	.1918
$m_t = 180$	94	.3048	.2986	.2897
	96	.3876	.3819	.3741
	98	.4589	.4537	.4467

(except in a complicated region of m_t near $M_Z/2$),

$$\delta A_{LR} \propto \frac{(m_t^2 - m_b^2)}{M_Z^2} \tag{9.8}$$

where m_b is the b quark mass. For very large top quark masses, $m_t \gg m_b$, M_Z, the shift in the asymmetry approaches the value

$$\delta A_{LR} \rightarrow \frac{4\sin^2\theta_w}{\left[1 + (1 - 4\sin^2\theta_w)^2\right]^2} \cdot \frac{\alpha}{\pi} \cdot N_c \cdot \left[\frac{m_t}{M_Z}\right]^2 \tag{9.9}$$

where N_c is the number of quark colors (three). The shift in the left-right asymmetry is shown in Figure 22 for various m_b/m_t ratios as a function of the top quark mass. Note that the effect does not vanish for unsplit doublets of arbitrarily large mass! This is certainly a surprise. Intuitively, we would expect that as the mass of a particle in a loop becomes larger, the mass terms in the propagator denominators cause it to *decouple* from the physics of the lower energy scale. It turns out that particles with axial vector couplings are permitted to violate our intuition as well as a mathematical theorem (the decoupling theorem). The asymptotic shift in A_{LR} caused by a very heavy degenerate quark isodoublet is given by the following expression,

$$\begin{aligned} \delta A_{LR} \rightarrow & -\frac{8N_c\sin^2\theta_w}{\left[1 + (1 - 4\sin^2\theta_w)^2\right]^2} \\ = & -0.004 \text{ for } \sin^2\theta_w = 0.230. \end{aligned} \tag{9.10}$$

Everything that has been said about the presence of largely split and unsplit quark doublets is also true for lepton doublets. The size of shift in the left-right asymmetry is reduced by the absence of a color factor. This is shown in Figure 23. The asymptotic shift in the asymmetry caused by the addition of a very heavy generation of quarks and leptons is $\delta A_{LR} \simeq -0.005$. The ultimate sensitivity of a measurement of A_{LR} will probably not permit strong statements about the presence of very heavy extra generations. However, it is conceivable that limits could be placed on extra heavy generations.

Other Asymmetries

The size of the virtual corrections to other asymmetries can be estimated from the corrections to A_{LR}. For example, the leptonic forward-backward asymmetry (without polarization) can be written as

$$A_{FB}^{l} = \frac{3}{4} \cdot A_{LR}^{2}.$$

The shift caused by the virtual corrections can be written as

$$\delta A_{FB}^{l} = \frac{3}{2} \cdot A_{LR} \cdot \delta A_{LR}.$$

We see that the shift caused by the *interesting* physics in the loop corrections is suppressed by a factor A_{LR}. This is especially important in the regime where the measurements are limited by statistics and the error on A_{FB}^{l} is absolute. It is ironic that A_{FB}^{l} is very sensitive to the very uninteresting initial state radiative corrections and is very insensitive to the interesting physics.

We note that the sensitivity of the polarized forward-backward asymmetry for leptons does not suffer from this disease.

9.2. Sensitivity To New Physics

We've just seen that the left-right asymmetry is sensitive to the top quark mass, the Higgs boson mass, and to extra doublets of quarks and leptons. How sensitive is it to other manifestations of new physics? Let's consider a few of the more popular topics.

Scalar Quarks and Leptons

Since supersymmetric quarks and leptons come in isodoublets, the argument of the last section about large splittings still applies. Indeed, if the mass of a squark or slepton is much larger than the mass of its partner and the Z° mass, then Equation (9.10) still applies (with m_t replaced by the mass of the heavy

SUSY particle, and N_c set the appropriate number of colors). Scalar particles do not, of course, have axial vector couplings. They must therefore decouple from the radiative corrections at high mass. The shift in A_{LR} for various mass splittings is shown as a function of the heavy particle mass in Figures 24 and 25 for scalar quarks and leptons, respectively. The effect can be large for widely split doublets.

Extra Z° Bosons

Extra Z° bosons are currently quite popular in theoretical circles. Most superstring motivated models involve the addition of at least one extra hypercharge-like degree of freedom. An extra neutral current is thus inevitable. Extra Z°'s have also been predicted by right-left symmetric models for some time. Additional neutral currents can contribute to the left-right asymmetry at tree level. Cvetic and Lynn[33] have considered the effects of both types of additional neutral currents on A_{LR}. The results of their calculations are shown in Figures 26 and 27 for the extra hypercharge and the broken right-left symmetric cases, respectively. In both cases, a measurement of A_{LR} would be sensitive to the presence of extra Z° bosons of mass up to $6 \rightarrow 7$ times the normal Z° mass.

10. Conclusions

We have seen that the measurement of the left-right polarization asymmetry at the Z° pole will be a powerful tool for testing the Standard Model. The use of polarized beams to enhance the forward-backward asymmetry will permit precision tests of lepton universality and measurements of the the Z°-heavy quark couplings. It was asserted that the polarized forward-backward asymmetries may greatly aid the separation of particles and antiparticles. The ability to control the spin degree of freedom of an electron or positron beam will be useful to the experimentalist and is likely to penetrate much of the physics to be done at the next generation of electron-positron colliders.

Acknowledgements:

The preparation of these lectures profited from several very helpful discussions with Bryan Lynn. My understanding of several of the less intuitive results was significantly improved from discussion with, and calculation by Michael Peskin. The structure, style, and content of this document have benefited greatly from the comments of Andreas Weigend, Frederic Perrier, and Ken Moffeit. I thank Eileen Brennan for her impressive patience and good nature while this document was being prepared and for her editorial skills once it was *complete.* The format of this document was significantly improved by the efforts of Lilian Vassilian. Finally, I thank David Leith for his helpful encouragement during the preparation of this manuscript.

REFERENCES

1. V. Bargmann, L. Michel, and V.L. Telegdi, Physical Review Letters **2**, 435 (1959).

2. J.D. Jackson, *Classical Electrodynamics, 2^{nd} Edition*, Wiley, New York, 1975.

3. L. T. Thomas, Phil. Mag. **3**, 1 (1927).

4. A nice review of low energy polarized electron sources is C.K. Sinclair, SLAC-PUB-3505, November 1984. Also published in *Proceedings of the 6^{th} International Symposium on High Energy Spin Physics, Marseille France*, edited by J. Soffer, Les Editions de Physique, Les Ulis France, 1985.

5. A good pedagogical review of polarized electron-positron storage rings is R.F. Schwitters, SLAC-PUB 2258, February 1979. Also published in *Proceedings of the 3^{rd} International Symposium on High Energy Physics with Polarized Beams and Targets, Argonne Il.*, edited by M.L. Marshak, American Institute of Physics, New York, 1976.

6. A more detailed review of polarization at storage rings is J. Buon, LAL/RT/86-02, March 1986.

7. G. Baym, *Lectures On Quantum Mechanics*, Benjamin, New York, 1975.

8. J. Kessler, *Polarized Electrons, 2^{nd} Edition*, Springer-Verlag, Berlin, 1985.

9. D.T. Pierce and F. Meier, Physical Review **B13**, 5484 (1976).

10. A.A. Sokolov and I.M Ternov, Soviet Physics-Dolkady **8**, 1203 (1964).

11. J.D. Jackson, Reviews of Modern Physics **48**, 417 (1976).

12. V.N. Baier and V.M. Katkov, Physics Letters **27A**, 327 (1967), and Soviet Physics-JETP **25**, 944 (1967).

13. The theory of spin dynamics in storage rings was originally done in Y.S. Derbenev and A.M. Kondratenko, Soviet Physics JETP **37**, 968 (1973).
More recent work is as follows:
A.W. Chao, Nuclear Instruments and Methods **180**, 29 (1981);
H. Mais and G. Ripkin, DESY 83-062, 1983;
S. Mane, Physical Review Letters **57**, 78 (1986);
L. Hand and A. Skuja, DESY 87-126, 1987.

14. B.W. Montague, CERN/ISR-TH/80-39, August 1980.
J. Buon and K. Steffen, Nuclear Instruments and Methods **A245**, 248 (1986).

15. N.F. Mott, *Proceedings of the Royal Society* A **124**, 425 (1929) and **135**, 429 (1932).

16. N.F. Mott and H.S.W. Massey, *The Theory of Atomic Collisions,* 3rd *Edition*, pg 238, Oxford University Press, Oxford.

17. N. Sherman, Physical Review **103**, 1601 (1956) and subsequent papers.

18. R.T. Cox, C.G. McIlwraith, and B. Kurrelmeyer, *Proceedings of the National Academy of Science* **14**, 544 (1928).

19. H. Frauenfelder and A. Rossi, Vol. 5, Part B, pg 243 of *Methods of Experimental Physics*, edited by I.C.L. Yuan and C.S. Wu, Academic Press, New York, 1963.

20. D.M. Schwartz, Physical Review **162**, 1806 (1967).

21. H. Bethe and W. Heitler, *Proceedings of the Royal Society* A **146**, 83 (1934).

22. See Reference 19 pg. 265.

23. See also C.Y. Prescott, SLAC-TN-73-1, January 1973.

24. A. Gongora and R.G. Stuart, Max Plank Institute preprint MPI-PAE/PTh-55/87, July 1987.

25. M. Böhm and W. Hollik, Nuclear Physics **B204**, 45 (1982).

26. B.W. Lynn and C. Verzegnassi, Physical Review **D35**, 3326 (1987).

27. A. Blondel, CERN EP-87/228, December 1987.

28. O. Nicosini and L. Trentadue, UPRF-86-132, December 1986.

29. A. Blondel, B.W. Lynn, F.M. Renard, and C. Verzegnassi, Montpellier preprint PM/87-14, March 1987.

30. D.C. Kennedy, B.W. Lynn, and C.J.-C. Im, SLAC-PUB-4128, March 1988.

31. See article in this proceeding by P. Grosse-Weismann and also W.B. Atwood, I. Dunietz, and P. Grosse-Weismann, SLAC-PUB-4544, April 1988.

32. B.W. Lynn, M.E. Peskin, and R.G. Stuart, SLAC-PUB-3725, June 1985.

33. M. Cvetic and B.W. Lynn, Physical Review **D36**, 51 (1987).

FIGURE CAPTIONS

1) The band structure of GaAs near the bandgap minimum (from references 9 and 4). The energy levels of the states are shown on the right. Allowed transitions for the absorption of right (left) circularly polarized photons are shown as solid (dashed) arrows. The circled numbers indicate the relative transition rates.

2) The band structure of Gallium Arsenide near its surface[9] for: (a) pure GaAs, (b) GaAs with a cesiated surface, and (c) GaAs with a layer of Cs_2O on its surface.

3) The polarization of electrons emitted from a GaAs photocathode as a function of photon wavelength and energy (from reference 4).

4) A comparision of the band structures of GaAs and the chalcopyrite semiconductor $CdSiAs_2$ (from reference 4).

5) The asymmetry function for mercury nuclei[16] is shown: (a) as a function of β for fixed scattering angle and (b) as a function of angle for fixed β.

6) A simplified Mott Polarimeter.

7) The 1928 experiment of Cox, McIlwraith, and Kurrelmeyer. A description of the apparatus can be found in the text.

8) The lowest order Feynman diagrams for (a) Bhabha Scattering and (b) Møller Scattering.

9) The unpolarized differential cross sections for Møller and Bhabha scattering are presented as a function of the center-of-mass scattering angle. The longitudinal and transverse asymmetry functions for both processes are also shown.

10) The beam's eye view of a Møller scattering target to be used at SLC. A holder containing four iron foils can be moved through the beam. Two foils are transverse to the beam and two are tilted at angle of 20° with respect

to the beam axis. A set of three Hemholz coils can produce a 100 gauss field along any of the three axes.

11) A schematical representation of a Møller polarimeter for the SLC extraction line.

12) The electron signal as measured in a Møller polarimeter. The top part of the figure shows the number of scattered electrons as a function of scattering angle. The signal appears at the angle that corresponds to the scattered momentum. The background is well described by the Bethe-Heitler process.

13) Feynman diagrams of the lowest order Compton scattering subprocesses.

14) The unpolarized cross section and the longitudinal and transverse polarization asymmetries are shown as a function of $x = K'/K'_{max}$ for the scattering of a 2.23 eV photon by a 46 GeV electron (y = 0.389).

15) A schematic diagram of a generic Compton polarimeter.

16) A layout of the SLAC Linear Collider. The orientation of an electron spin vector is shown as the electron is transported from the electron gun to the interaction point.

17) The electron-positron coordinate system. The electron beam is moving in the +z direction. The x-axis points in the horizontal direction and the y-axis in the vertical direction. The electron and positron longitudinal polarizations are described in terms of a helicity basis. Right-handed particles (and antiparticles) have $\mathcal{P}_z = +1$ and left-handed particles have $\mathcal{P}_z = -1$.

18) The leptonic forward-backward asymmetry and the left-right asymmetry are shown as functions of $\sin^2\theta_w$ and M_Z.

19) The expected uncertainty of a measurement of the left-right asymmetry A_{LR} as a function of the number of events used. The beam polarization is taken to be 45%. The Z° mass is assumed to be 92.5 GeV. The corresponding uncertainty on $\sin^2\theta_w$ and on the mass of the Z° is also shown. The expected and achieved precision of several other measurements

is also shown. The expected precision on $\sin^2\theta_w$ from a measurement of the leptonic forward-backward asymmetry with zero polarization is shown for comparison.

20) The energy dependence of the forward-backward asymmetry A_{FB}^f (polarized and otherwise), the improved forward-backward asymmetry $\tilde{A}_{FB}^f$, and the left-right asymmetry A_{LR} for several final state fermions. Note that the unimproved forward-backward asymmetries are much more sensitive to the center-of-mass energy than are the improved ones and the left-right asymmetries.

21) Several calculations[32] of the left-right asymmetry are shown as functions of $\sqrt{s}$. The tree-level expressions for M_Z = 98 GeV, 94 GeV, 90 GeV are shown as dashed curves. The application of of the photon vacuum polarization correction is shown for each value of M_Z by the dotted curve. The fully corrected asymmetry is shown as a solid line for each mass value. The top quark mass is assumed to be 30 GeV and the Higgs mass is taken to be 100 GeV.

22) The shift in the left-right asymmetry caused by the addition of quark doublets of various mass splittings.[32] The effect increases with the size of the mass splitting but does not vanish for unsplit doublets.

23) The shift in the left-right asymmetry caused by the addition of lepton doublets of various mass splittings.[32] The effect is largest for largely split doublets but does not vanish for unsplit doublets.

24) The shift in the left-right asymmetry caused by the addition of scalar quark doublets of various mass splittings.[32]

25) The shift in the left-right asymmetry caused by the addition of scalar lepton doublets of various mass splittings.[32]

26) The effect of an extra Z° boson on the left-right asymmetry as a function of its mass (from Reference 33). The extra Z° is due to an additional U(1)

hypercharge-like group. The different curves correspond to different choices of parameters.

27) The effect of an extra Z° boson on the left-right asymmetry as a function of its mass (from Reference 33). The extra Z° is due to the breaking of a right-left symmetric model. The different curves correspond to different choices of parameters.

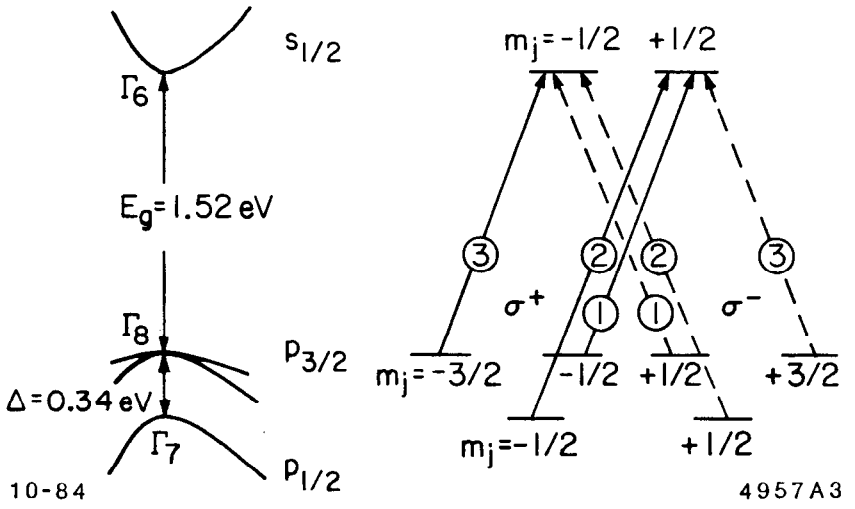

Fig. 1. The band structure of GaAs near the bandgap minimum (from References 4 and 9). The energy levels of the states are shown on the right. Allowed transitions for the absorption of right (left) circularly polarized photons are shown as solid (dashed) arrows. The circled numbers indicate the relative transition rates.

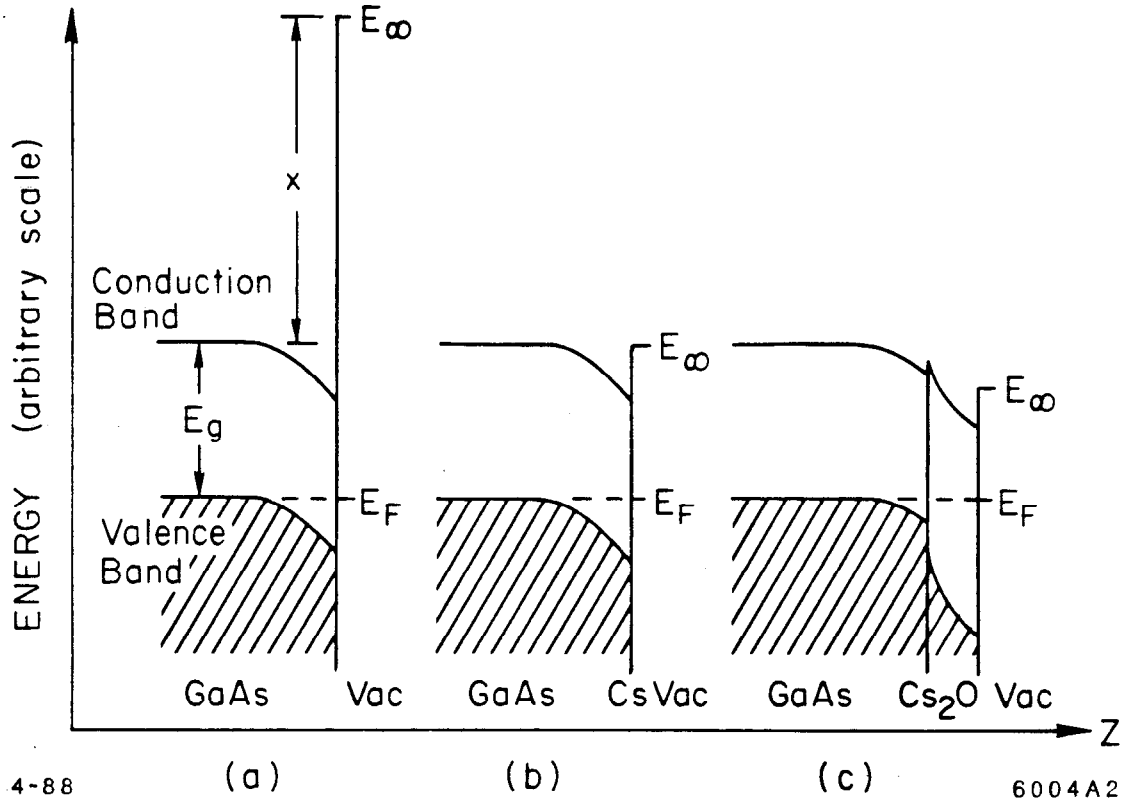

Fig. 2. The band structure of Gallium Arsenide near its surface[9] for: (a) pure GaAs, (b) GaAs with a cesiated surface, and (c) GaAs with a layer of Cs_2O on its surface.

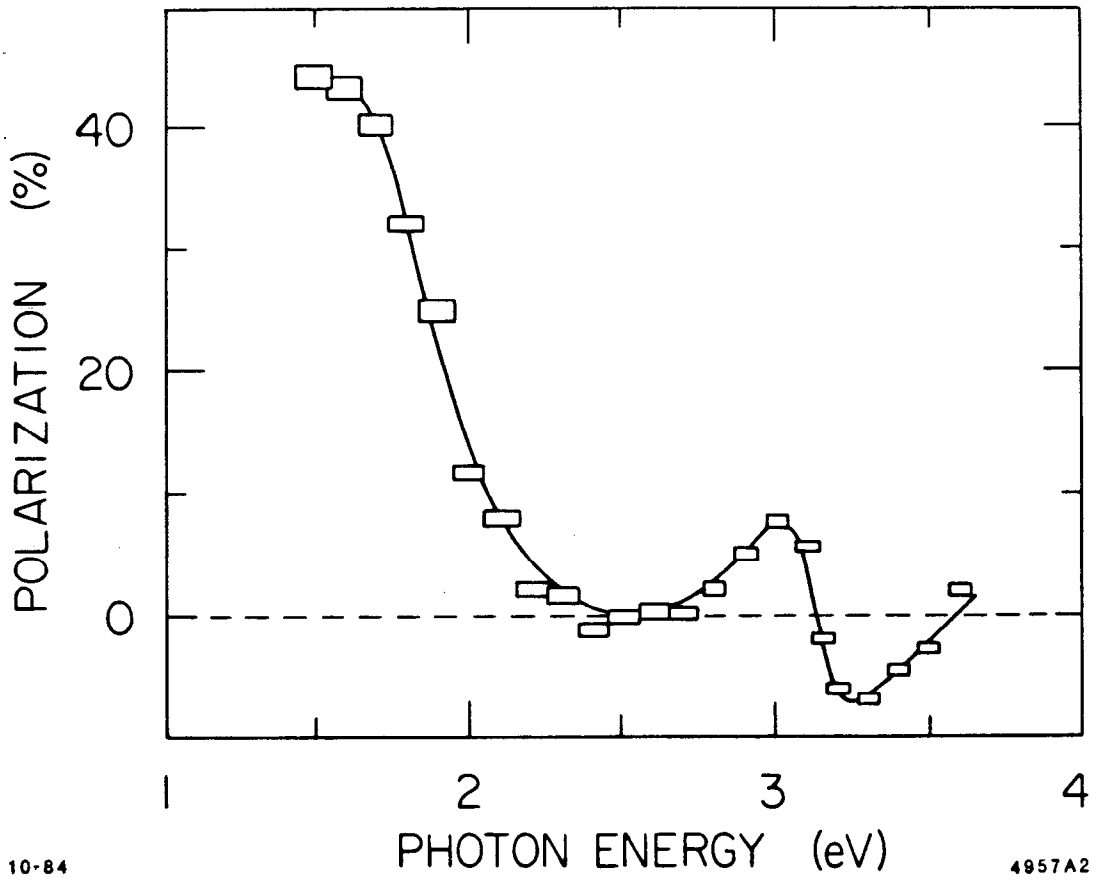

Fig. 3. The polarization of electrons emitted from a GaAs photocathode as a function of photon wavelength and energy (from Reference 4).

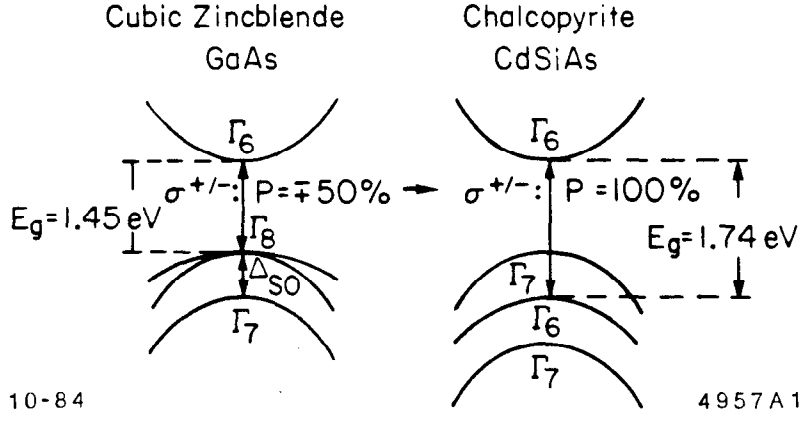

Fig. 4. A comparison of the band structures of GaAs and the chalcopyrite semiconductor $CdSiAs_2$ (from Reference 4).

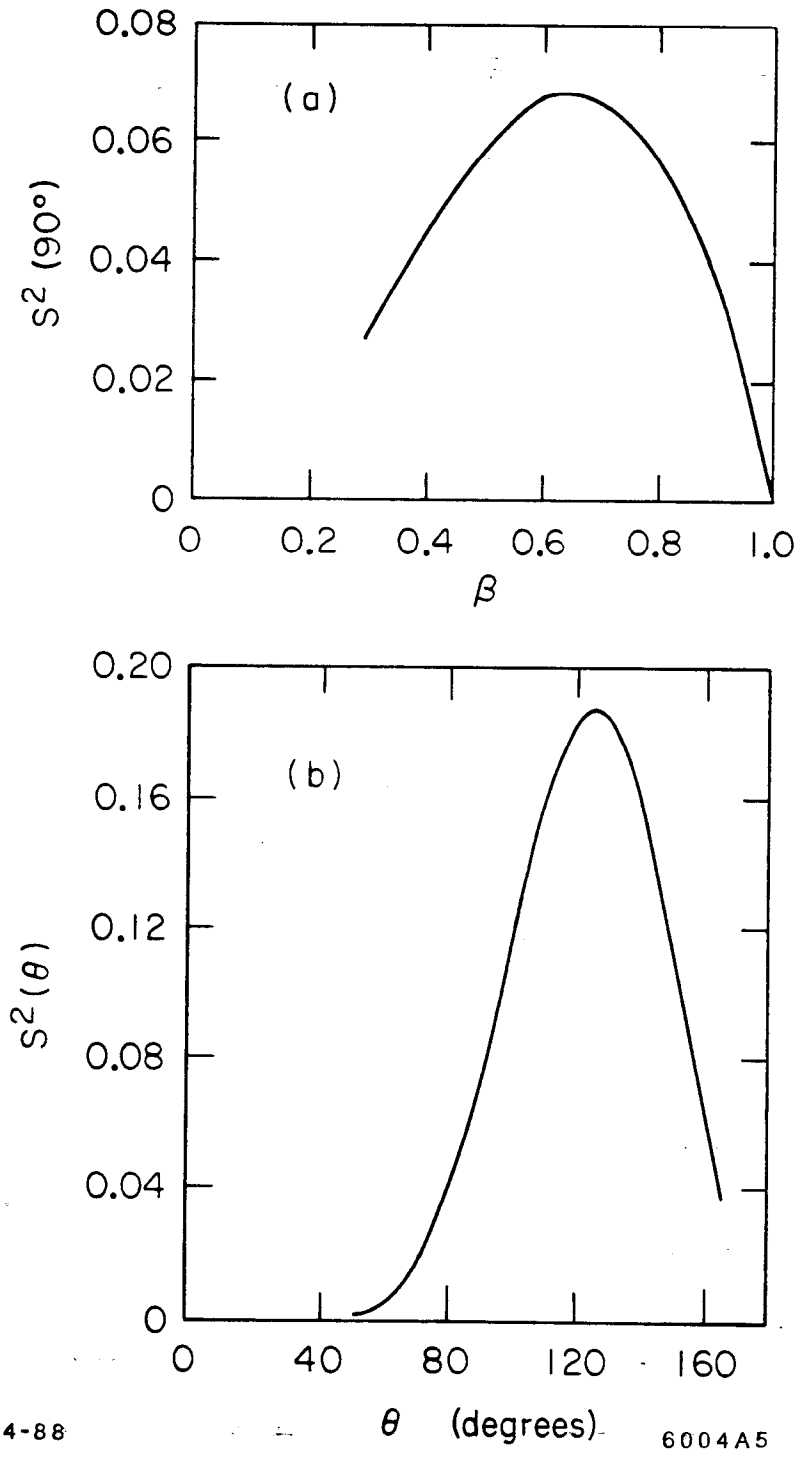

Fig. 5. The asymmetry function for mercury nuclei[16] is shown: (a) as a function of β for fixed scattering angle and (b) as a function of angle for fixed β.

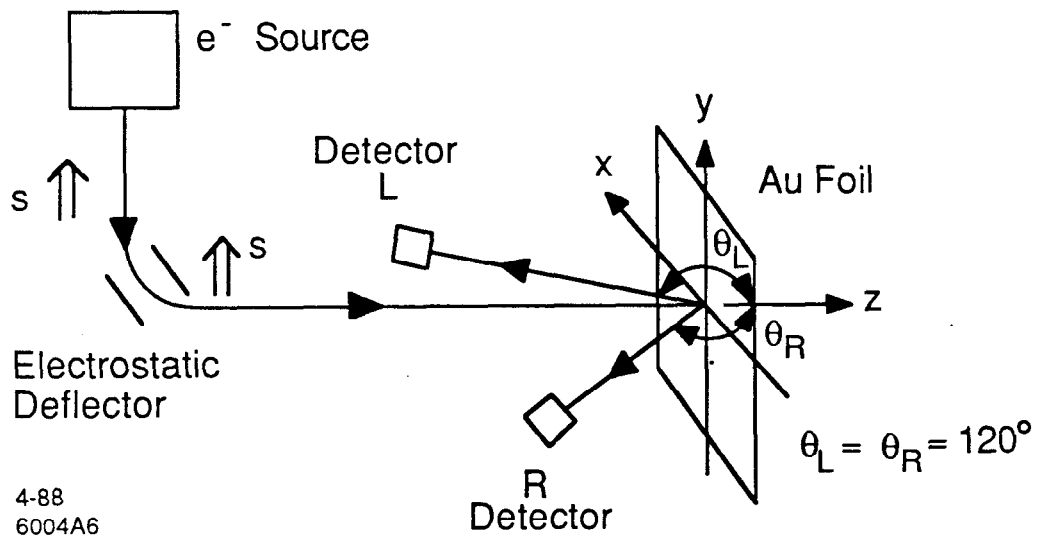

Fig. 6. A simplified Mott Polarimeter.

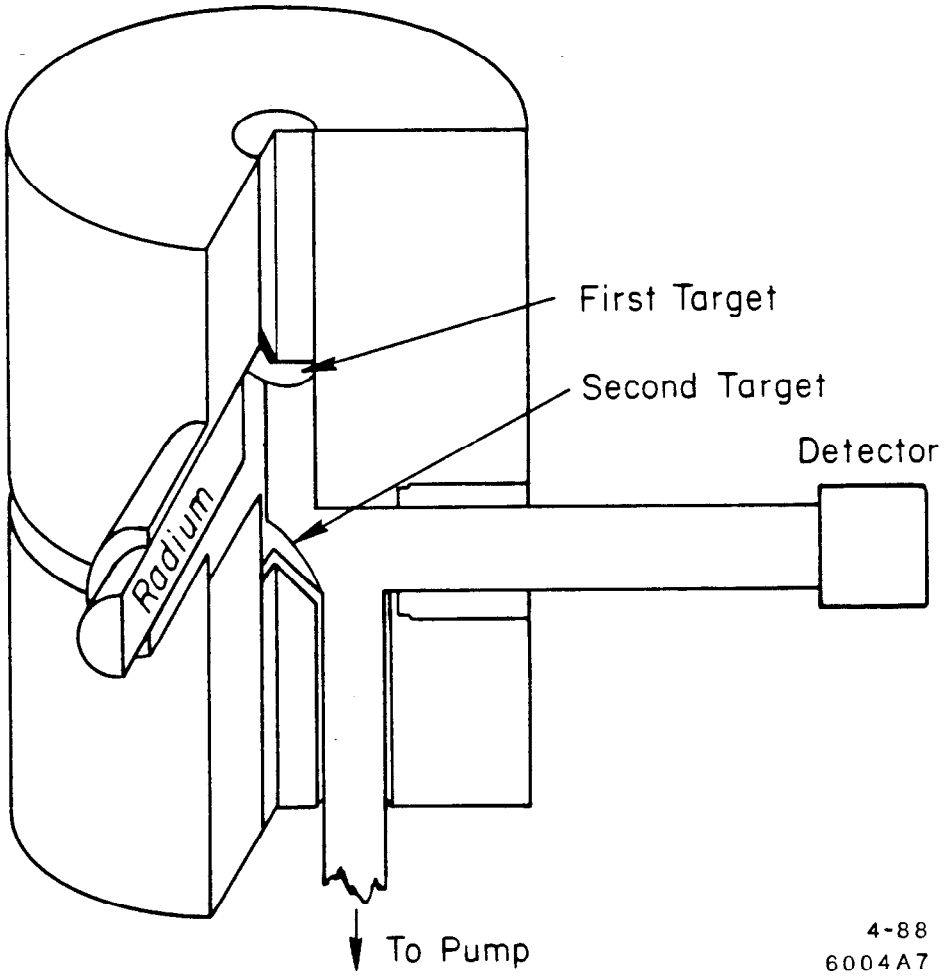

Fig. 7. The 1928 experiment of Cox, McIlwraith, and Kurrelmeyer. A description of the apparatus can be found in the text.

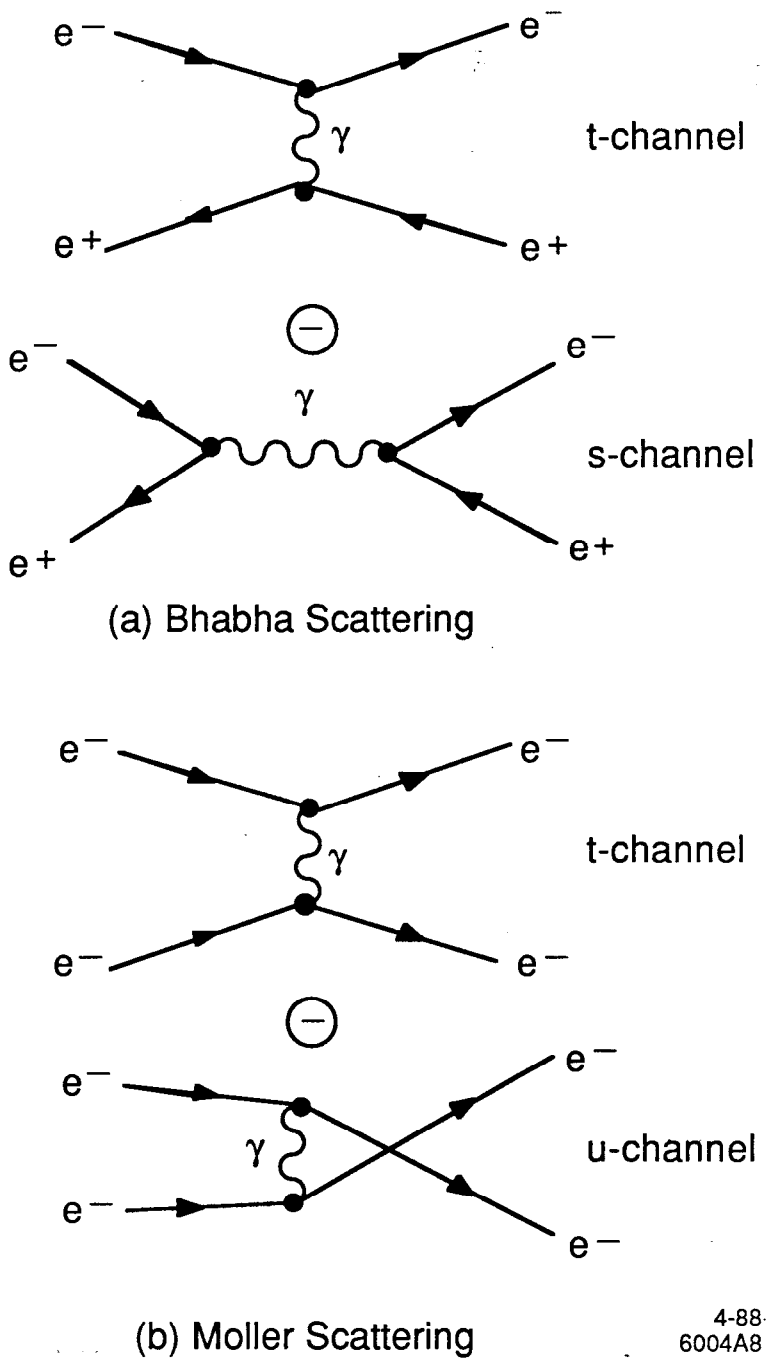

Fig. 8. The lowest order Feynman diagrams for (a) Bhabha Scattering and (b) Møller Scattering.

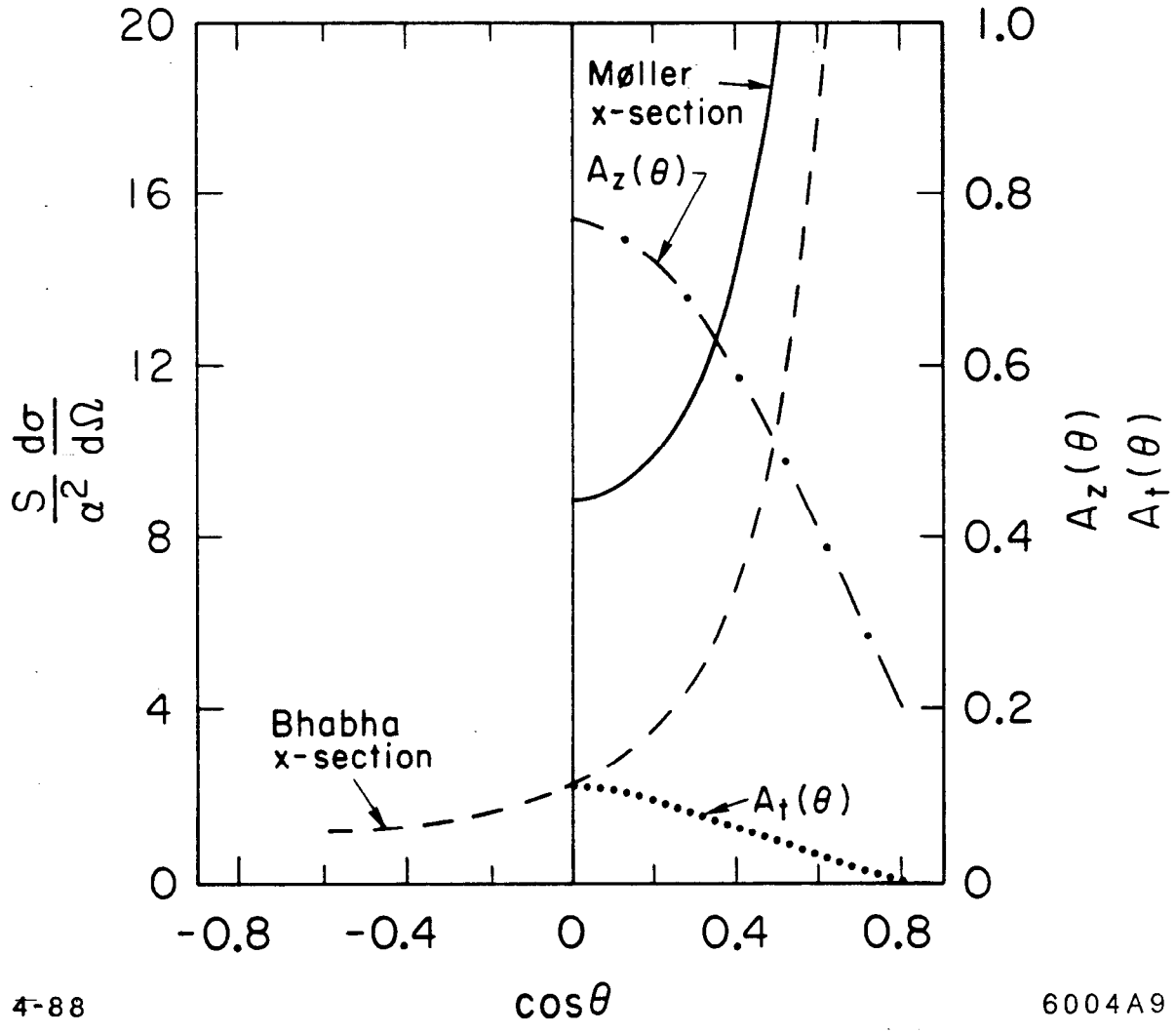

Fig. 9. The unpolarized differential cross sections for Møller and Bhabha scattering are presented as a function of the center-of-mass scattering angle. The longitudinal and transverse asymmetry functions for both processes are also shown.

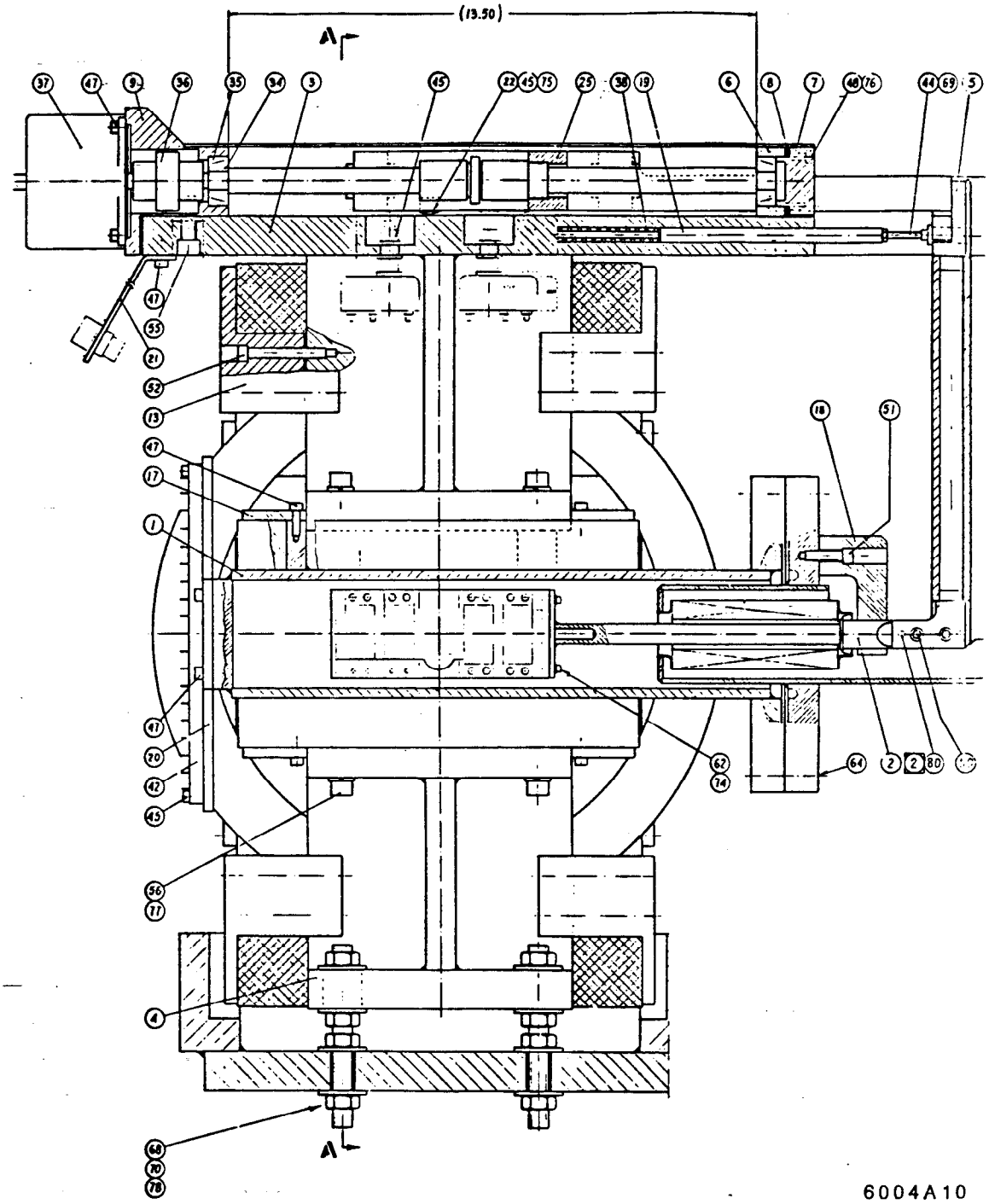

Fig. 10. The beam's eye view of a Møller scattering target to be used at SLC. A holder containing four iron foils can be moved through the beam. Two foils are transverse to the beam and two are tilted at angle of 20° with respect to the beam axis. A set of three Hemholz coils can produce a 100 gauss field along any of the three axes.

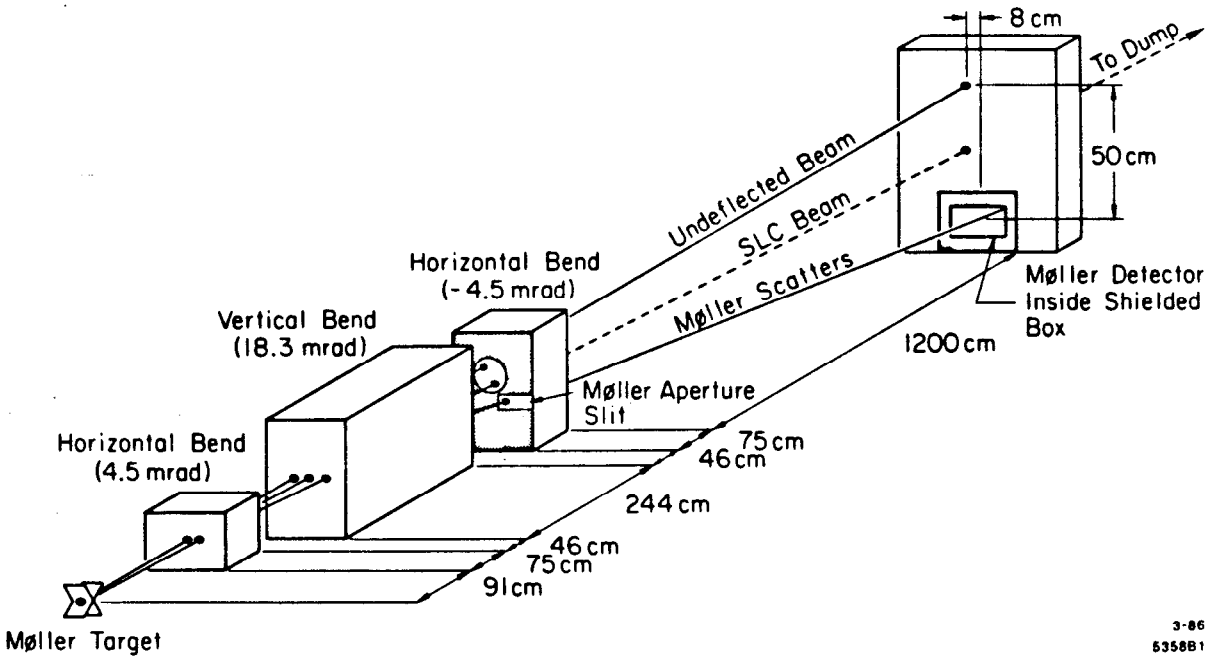

Fig. 11. A schematical representation of a Møller polarimeter for the SLC extraction line.

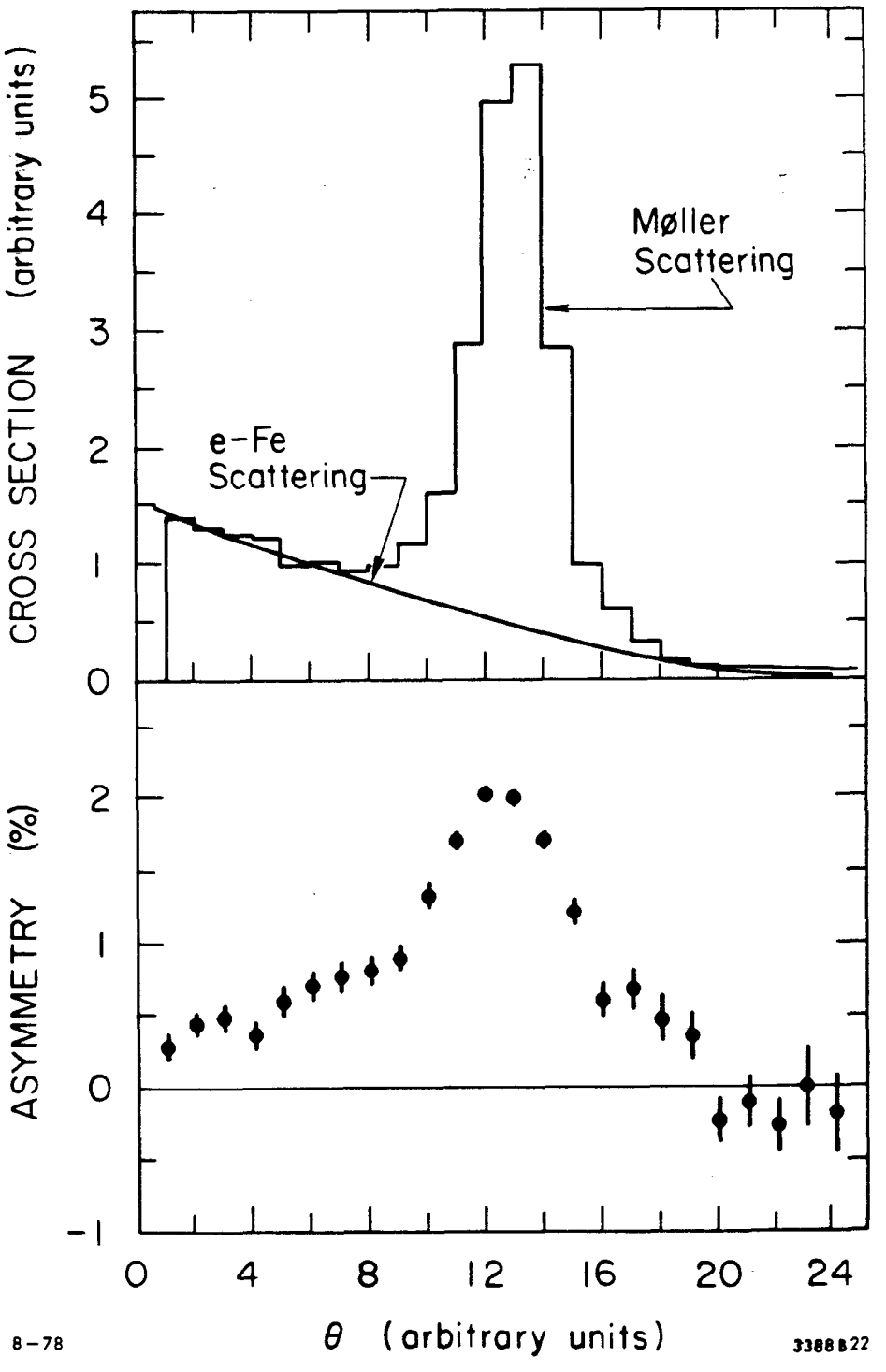

Fig. 12. The electron signal as measured in a Møller polarimeter. The top part of the figure shows the number of scattered electrons as a function of scattering angle. The signal appears at the angle that corresponds to the scattered momentum. The background is well described by the Bethe-Heitler process.

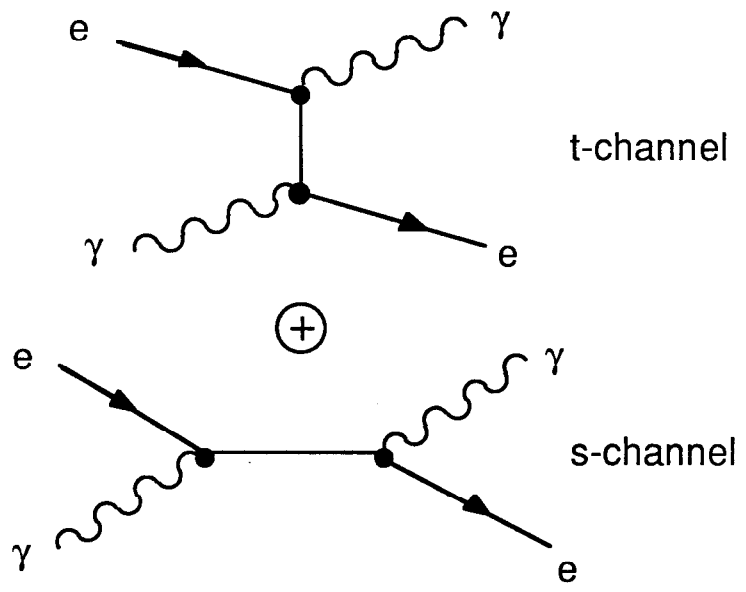

Fig. 13. Feynman diagrams of the lowest order Compton scattering subprocesses.

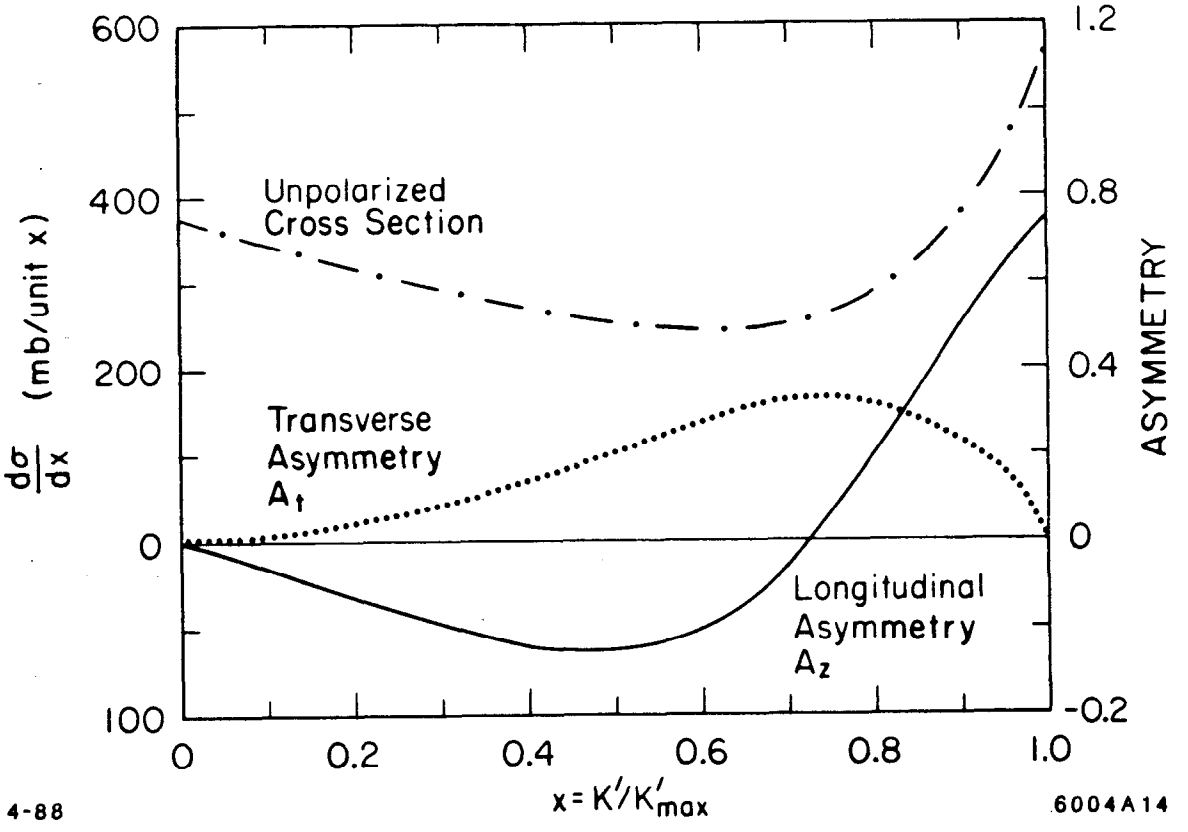

Fig. 14. The unpolarized cross section and the longitudinal and transverse polarization asymmetries are shown as a function of $x = K'/K'_{max}$ for the scattering of a 2.23 eV photon by a 46 GeV electron (y = 0.389).

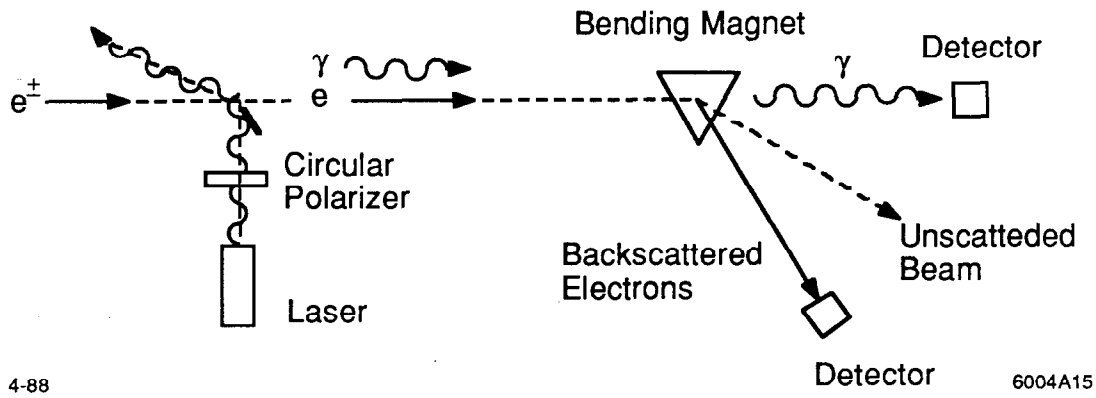

Fig. 15. A schematic diagram of a generic Compton polarimeter.

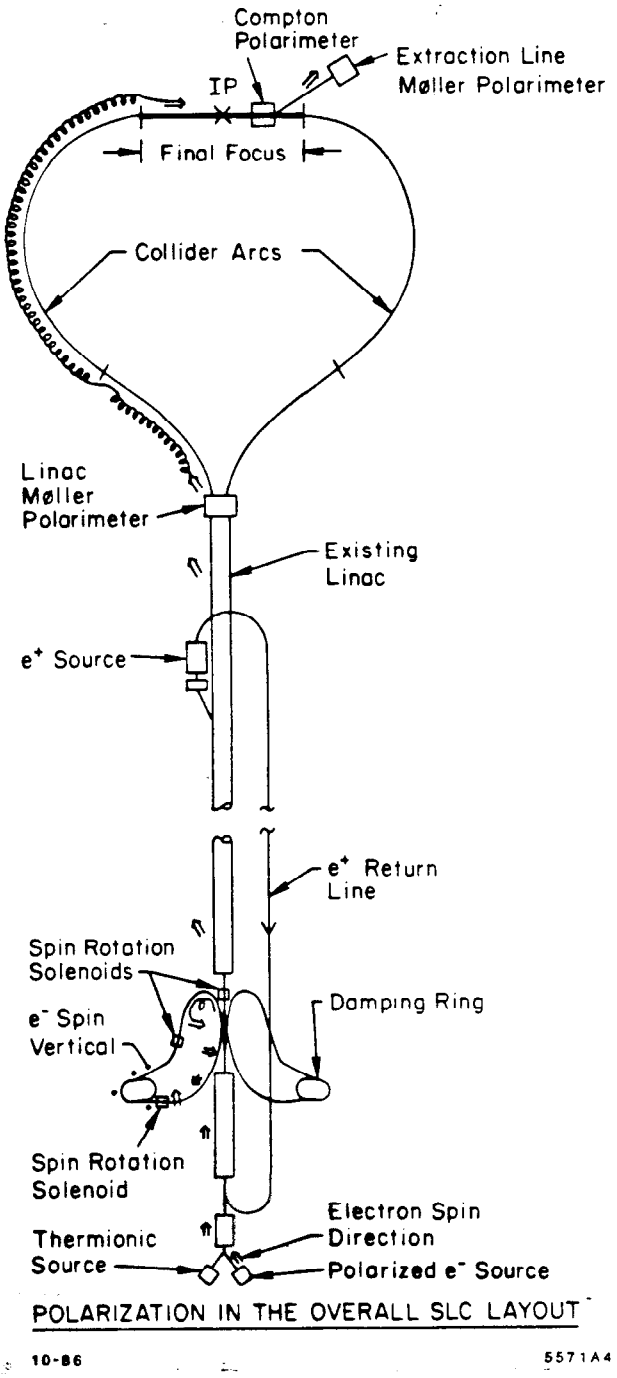

Fig. 16. A layout of the SLAC Linear Collider. The orientation of an electron spin vector is shown as the electron is transported from the electron gun to the interaction point.

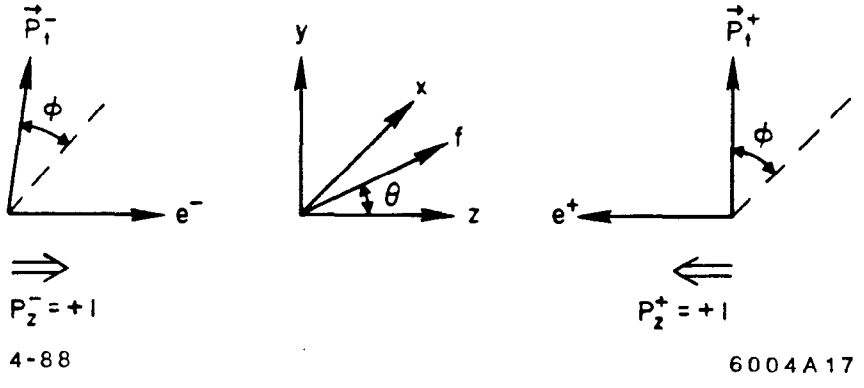

Fig. 17. The electron-positron coordinate system. The electron beam is moving in the +z direction. The x-axis points in the horizontal direction and the y-axis in the vertical direction. The electron and positron longitudinal polarizations are described in terms of a helicity basis. Right-handed particles (and antiparticles) have $P_z = +1$ and left-handed particles have $P_z = -1$.

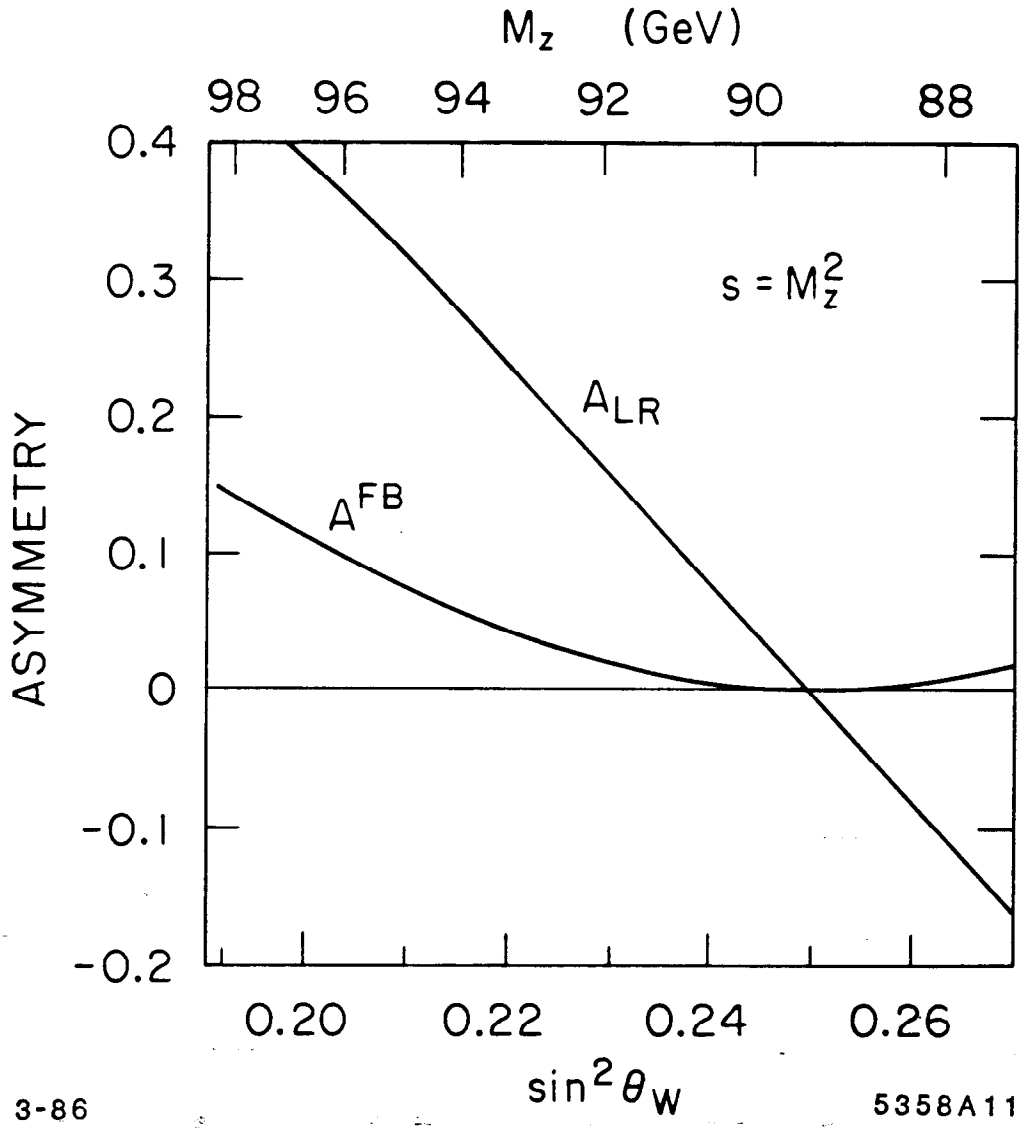

Fig. 18. The leptonic forward-backward asymmetry and the left-right asymmetry are shown as functions of $\sin^2\theta_w$ and M_Z.

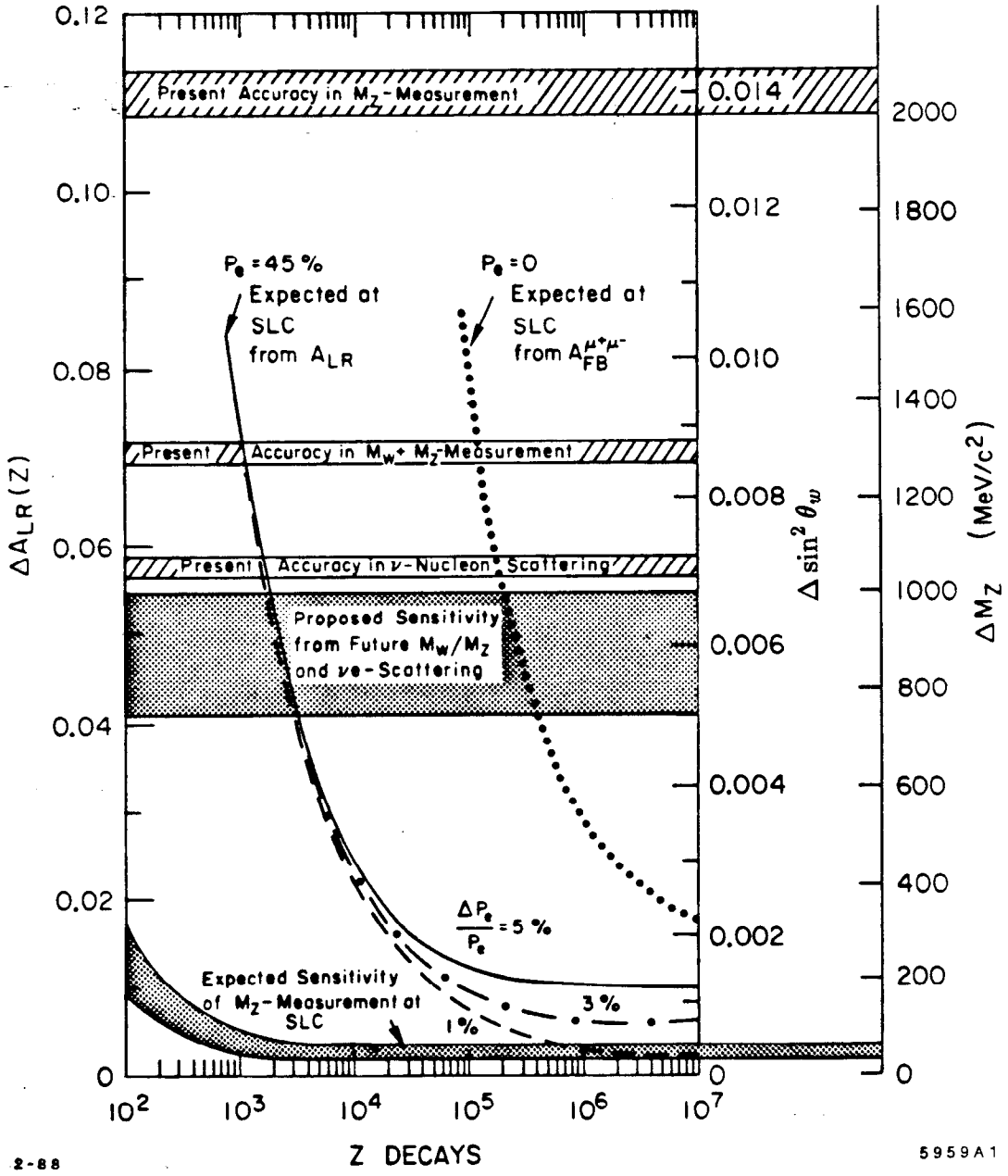

Fig. 19. The expected uncertainty of a measurement of the left-right asymmetry A_{LR} as a function of the number of events used. The beam polarization is taken to be 45%. The Z° mass is assumed to be 92.5 GeV. The corresponding uncertainty on $\sin^2\theta_w$ and on the mass of the Z° is also shown. The expected and achieved precision of several other measurements is also shown. The expected precision on $\sin^2\theta_w$ from a measurement of the leptonic forward-backward asymmetry with zero polarization is shown for comparison.

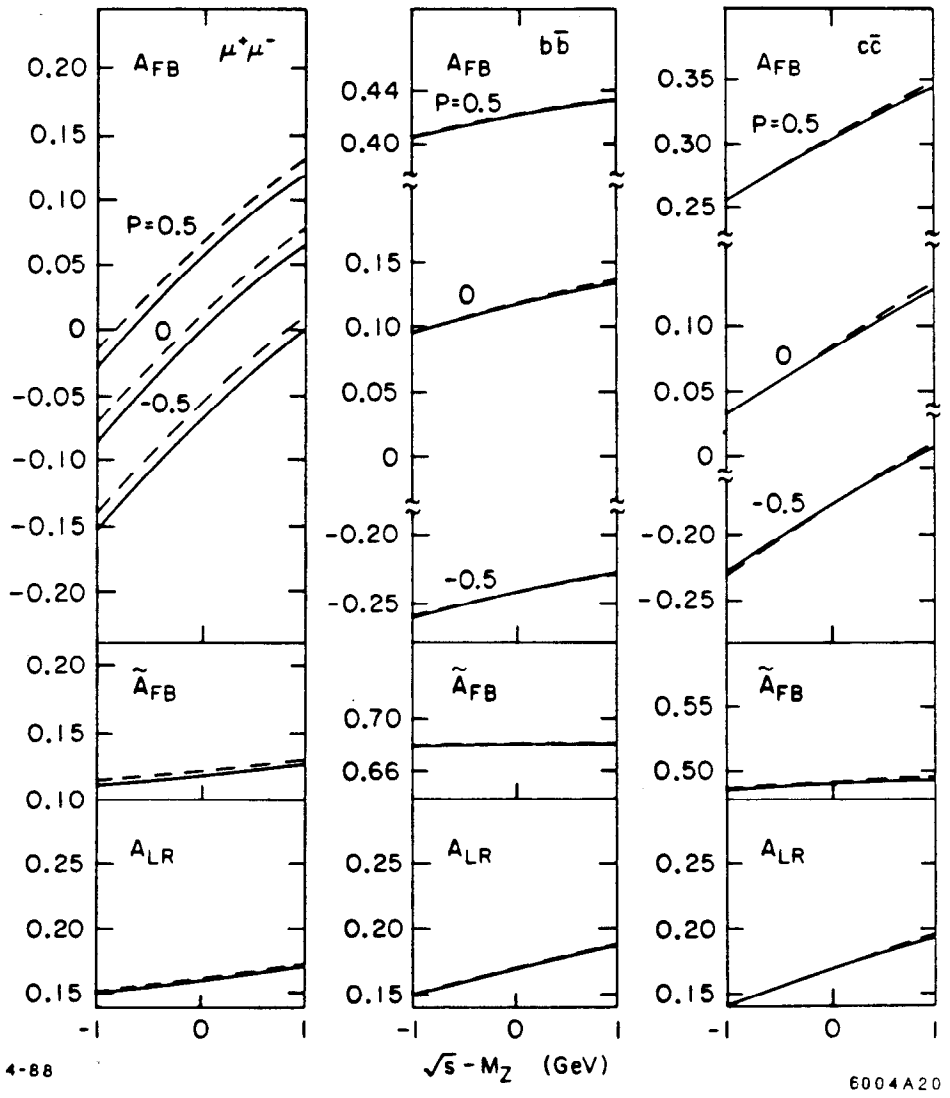

Fig. 20. The energy dependence of the forward-backward asymmetry A_{FB}^f (polarized and otherwise), the improved forward-backward asymmetry $\tilde{A}_{FB}^f$, and the left-right asymmetry A_{LR} for several final state fermions. Note that the unimproved forward-backward asymmetries are much more sensitive to the center-of-mass energy than are the improved ones and the left-right asymmetries.

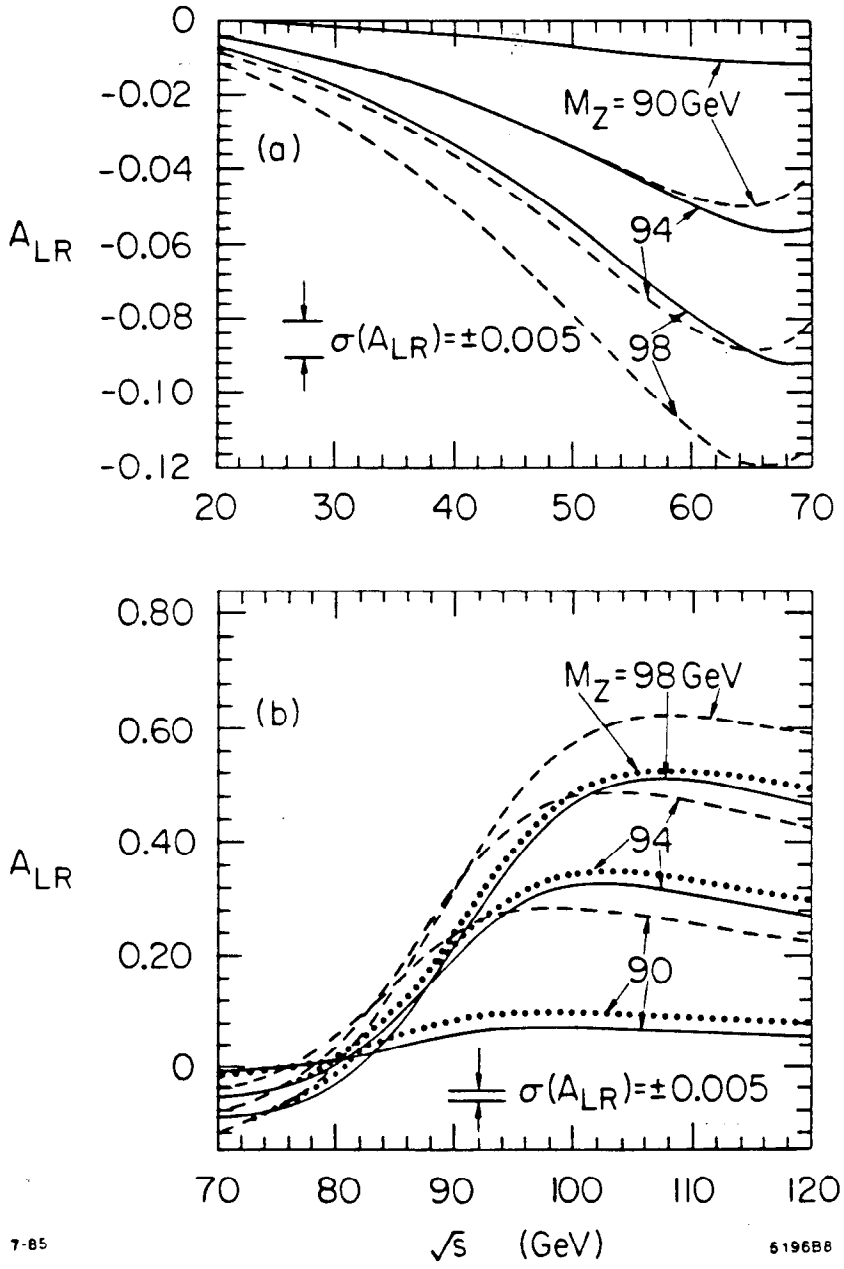

Fig. 21. Several calculations[31] of the left-right asymmetry are shown as functions of $\sqrt{s}$. The tree-level expressions for M_Z = 98 GeV, 94 GeV, 90 GeV are shown as dashed curves. The application of of the photon vacuum polarization correction is shown for each value of M_Z by the dotted curve. The fully corrected asymmetry is shown as a solid line for each mass value. The top quark mass is assumed to be 30 GeV and the Higgs mass is taken to be 100 GeV.

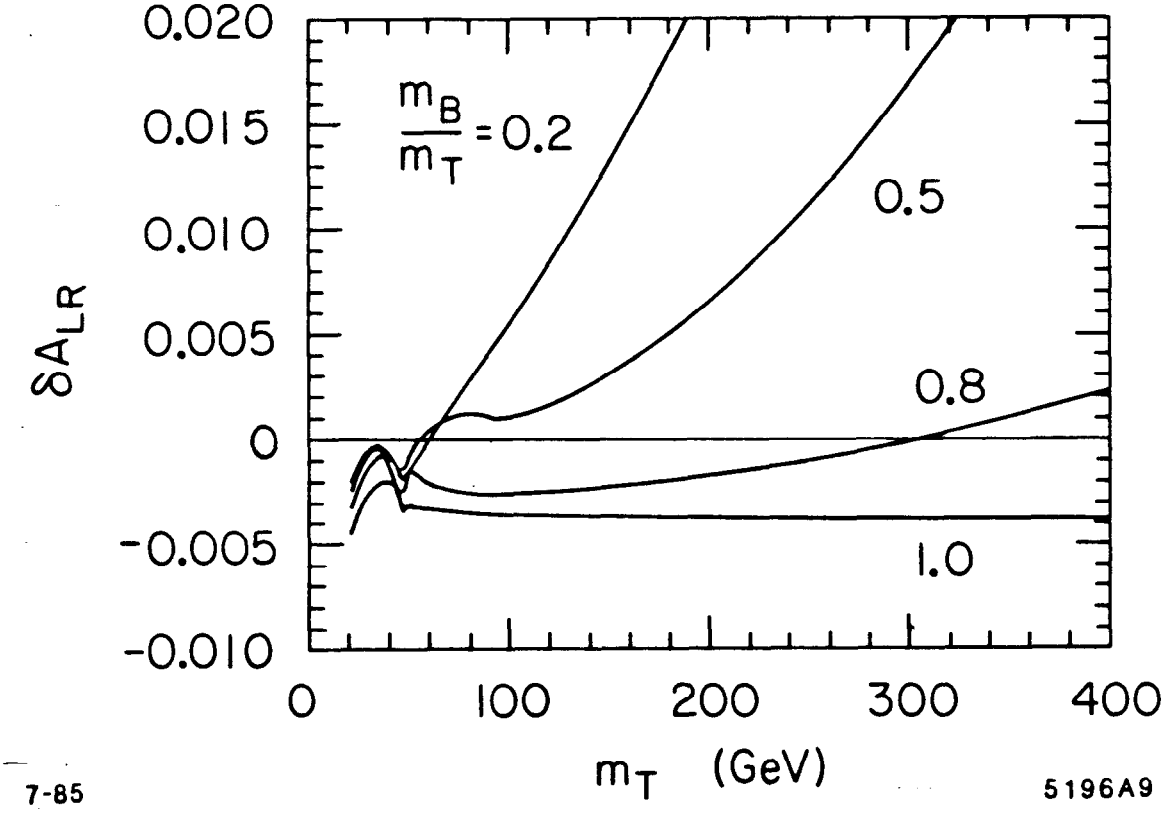

Fig. 22. The shift in the left-right asymmetry caused by the addition of quark doublets of various mass splittings.[31] The effect increases with the size of the mass splitting but does not vanish for unsplit doublets.

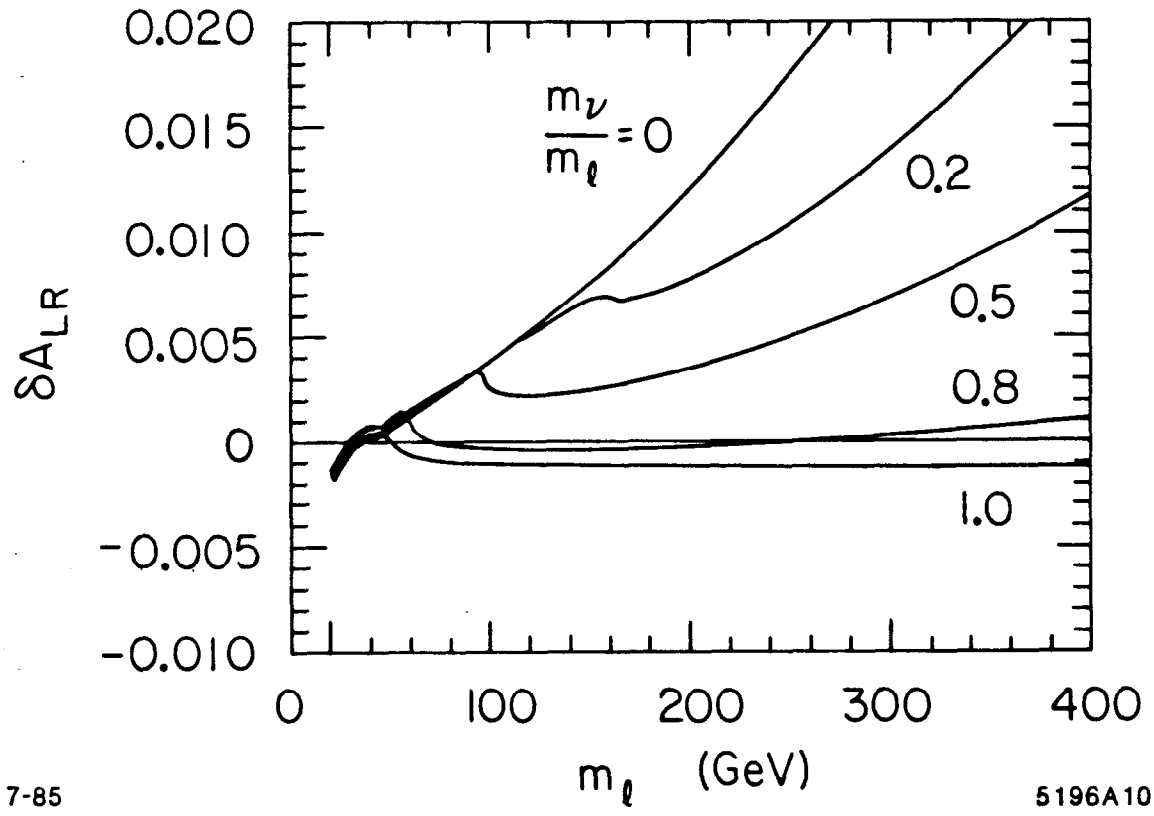

Fig. 23. The shift in the left-right asymmetry caused by the addition of lepton doublets of various mass splittings.[31] The effect is largest for largely split doublets but does not vanish for unsplit doublets.

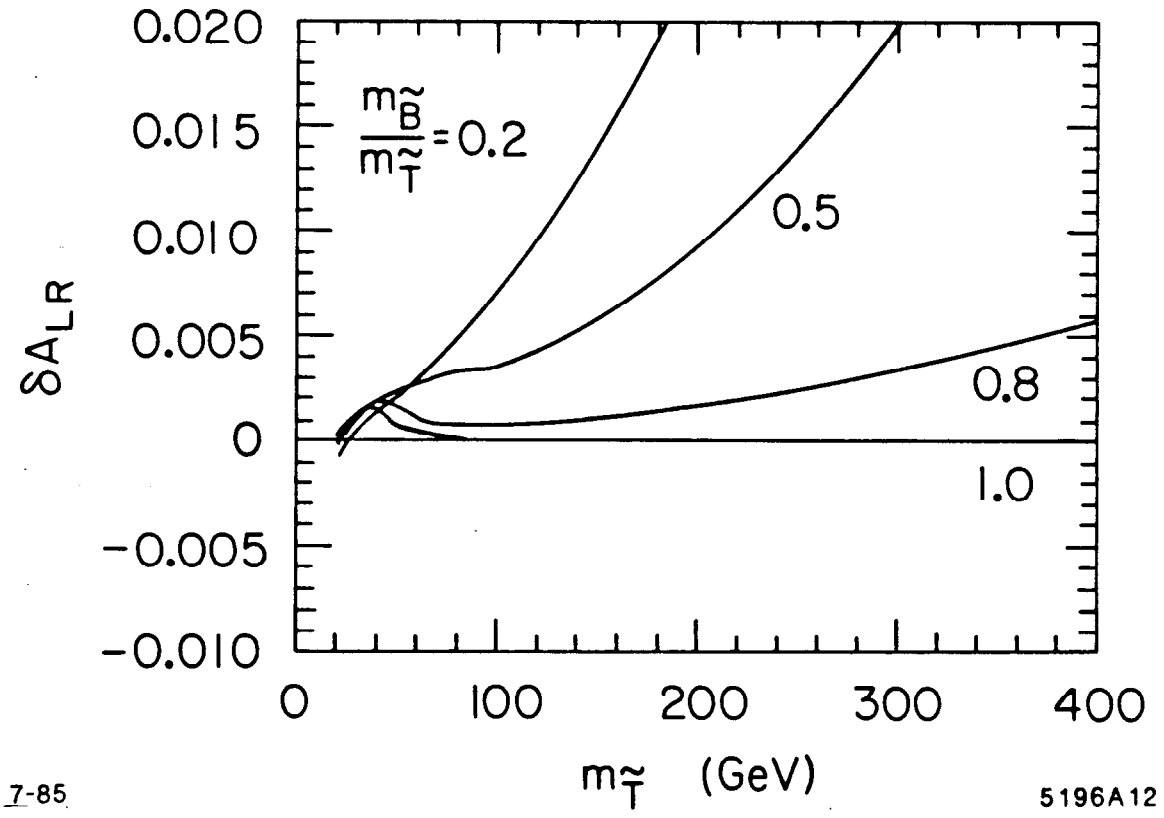

Fig. 24. The shift in the left-right asymmetry caused by the addition of scalar quark doublets of various mass splittings.[31]

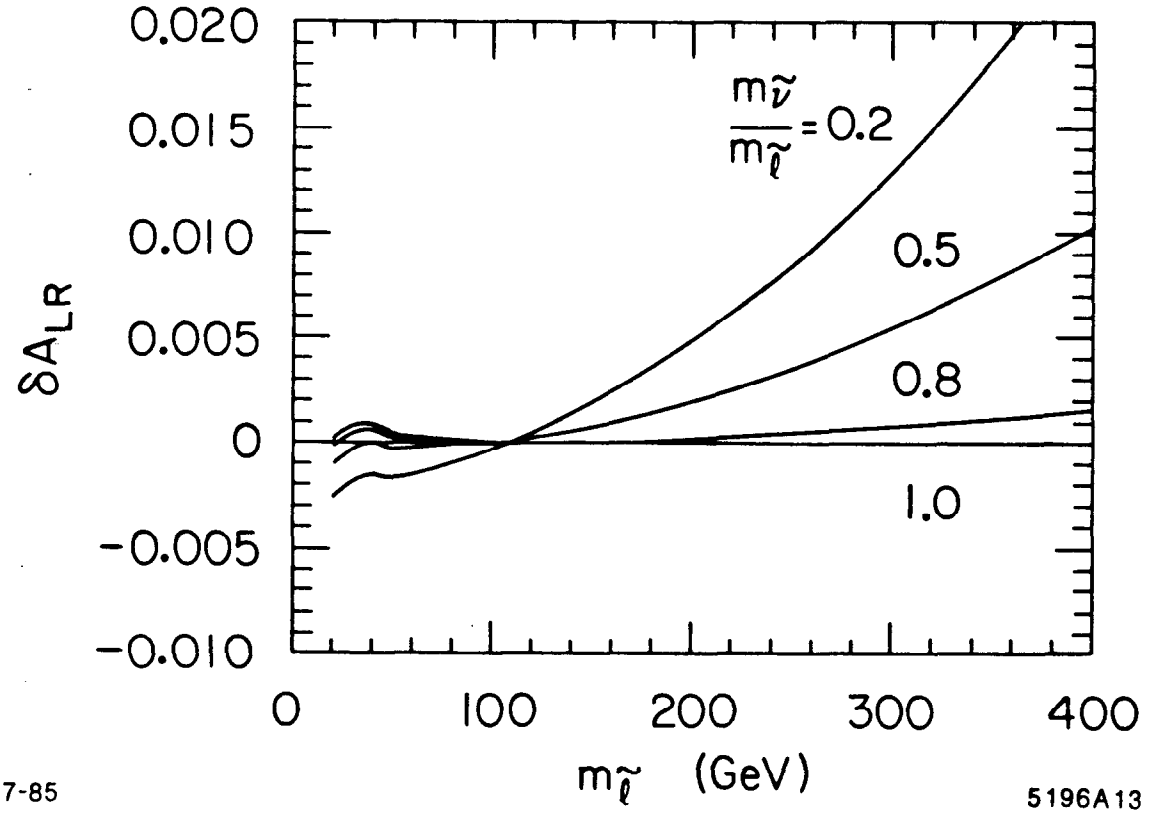

Fig. 25. The shift in the left-right asymmetry caused by the addition of scalar lepton doublets of various mass splittings.[31]

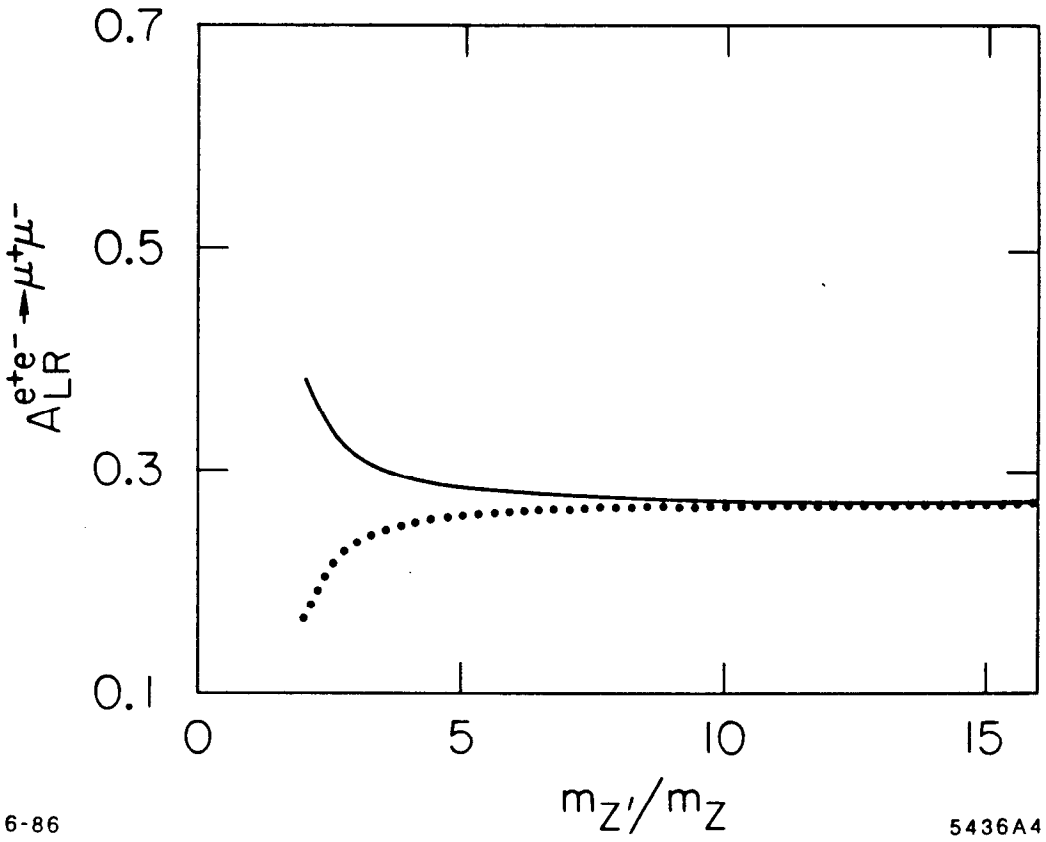

Fig. 26. The effect of an extra Z° boson on the left-right asymmetry as a function of its mass (from Reference 32). The extra Z° is due to an additional U(1) hypercharge-like group. The different curves correspond to different choices of parameters.

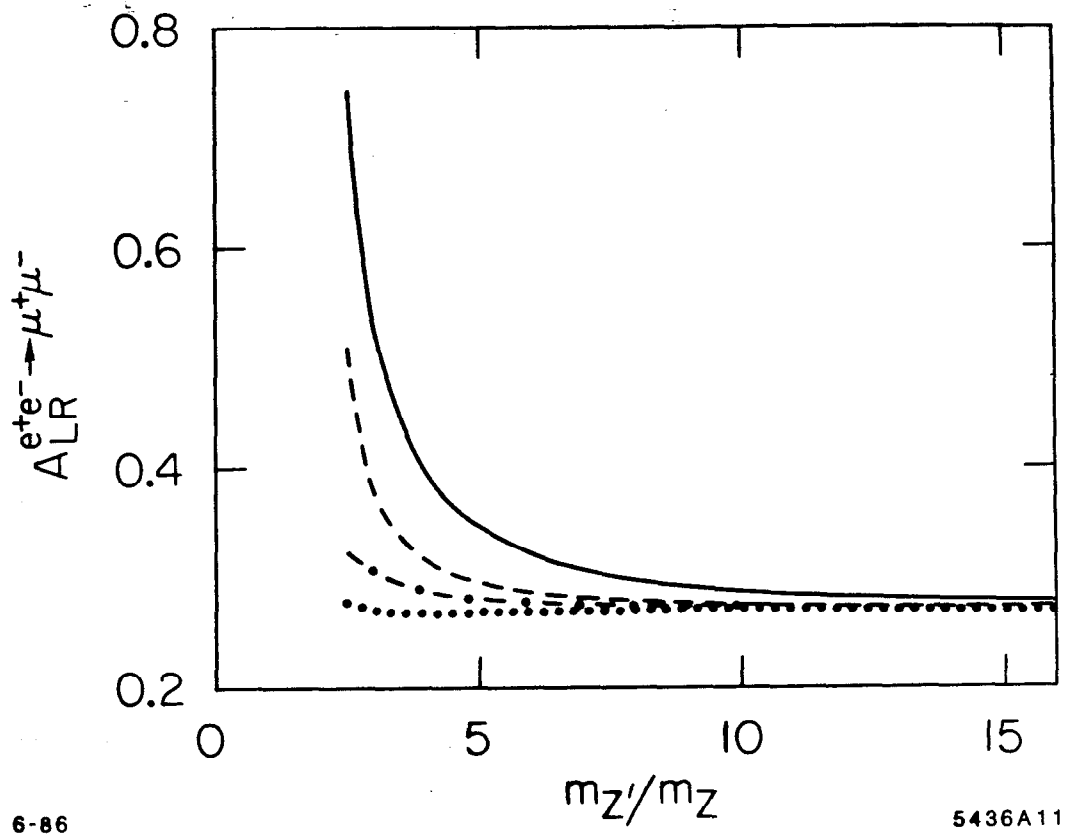

Fig. 27. The effect of an extra Z° boson on the left-right asymmetry as a function of its mass (from Reference 32). The extra Z° is due to the breaking of a right-left symmetric model. The different curves correspond to different choices of parameters.